JGR Oceans

RESEARCH ARTICLE
10.1029/2020JC016962

Key Points:

- Overturning maximum is 15.64 ± 1.39 Sv; Meridional heat and freshwater transport are 0.27 ± 0.10 PW and 0.23 ± 0.02 Sv, respectively
- Excluding the mesoscale eddies from the section increased the meridional heat transport by 0.12 PW
- The distribution of water masses and currents reflects the favorable position of the section for observing

Supporting Information:

- Supporting Information S1

Correspondence to:
G. Manta,
gaston.manta@lmd.ens.fr

Citation:
Manta, G., Speich, S., Karstensen, J., Hummels, R., Kersalé, M., Laxenaire, R., et al. (2021). The South Atlantic meridional overturning circulation and mesoscale eddies in the first GO-SHIP section at 34.5°S. *Journal of Geophysical Research: Oceans*, *126*, e2020JC016962. https://doi.org/10.1029/2020JC016962

Received 7 NOV 2020
Accepted 21 DEC 2020

The South Atlantic Meridional Overturning Circulation and Mesoscale Eddies in the First GO-SHIP Section at 34.5°S

G. Manta[1,2], S. Speich[1], J. Karstensen[3], R. Hummels[3], M. Kersalé[4,5], R. Laxenaire[6], A. Piola[7,8,9,10], M. P. Chidichimo[7,9,10], O. T. Sato[11], L. Cotrim da Cunha[12], I. Ansorge[13], T. Lamont[13,14,15], M.A. van den Berg[14], U. Schuster[16], T. Tanhua[3], R. Kerr[17], R. Guerrero[18], E. Campos[11,19], and C. S. Meinen[5]

[1]Laboratoire de Météorologie Dynamique, LMD-IPSL, École Polytechnique, ENS, CNRS, Paris, France, [2]Departamento de Ciencias de la Atmósfera, Facultad de Ciencias, Universidad de la República, Montevideo, Uruguay, [3]GEOMAR Helmholtz Centre for Ocean Research Kiel, Kiel, Germany, [4]Cooperative Institute for Marine and Atmospheric Studies, University of Miami, Miami, FL, USA, [5]NOAA Atlantic Oceanographic and Meteorological Laboratory, Miami, FL, USA, [6]Center for Ocean-Atmospheric Prediction Studies, Florida State University, Tallahassee, FL, USA, [7]Departamento de Oceanografía, Servicio de Hidrografía Naval (SHN), Buenos Aires, Argentina, [8]Departamento de Ciencias de la Atmósfera y los Océanos, Universidad de Buenos Aires, Buenos Aires, Argentina, [9]Consejo Nacional de Investigaciones Científicas y Técnicas, Buenos Aires, Argentina, [10]Instituto Franco-Argentino Sobre Estudios de Clima y Sus Impactos, CNRS-CONICET-UBA, Buenos Aires, Argentina, [11]Oceanographic Institute, University of São Paulo, São Paulo, Brazil, [12]Faculdade de Oceanografia, BrOA, Universidade do Estado do Rio de Janeiro, Rio de Janeiro, Brazil, [13]Oceanography Department, University of Cape Town, Cape Town, South Africa, [14]Department of Environment, Forestry and Fisheries, Oceans & Coasts Research Branch, Cape Town, South Africa, [15]Bayworld Centre for Research and Education, Cape Town, South Africa, [16]College of Life and Environmental Sciences, University of Exeter, Exeter, UK, [17]Laboratório de Estudos dos Oceanos e Clima, Instituto de Oceanografia, Universidade Federal do Rio Grande—FURG, Rio Grande, Brazil, [18]Departamento de Ciencias Marinas, Facultad de Ciencias Exactas y Naturales, Universidad Nacional de Mar del Plata, Funes, Argentina, [19]Department of Biology, Chemistry and Environmental Sciences, College of Arts and Sciences, American University of Sharjah, Sharjah, United Arab Emirates

Abstract The variability of the Atlantic meridional overturning circulation (AMOC) has considerable impacts on the global climate system. Past studies have shown that changes in the South Atlantic control the stability of the AMOC and drive an important part of its variability. That is why significant resources have been invested in a South (S)AMOC observing system. In January 2017, the *RV Maria S. Merian* conducted the first GO-SHIP hydrographic transect along the SAMOC-Basin Wide Array (SAMBA) line at 34.5°S in the South Atlantic. This paper presents estimates of meridional volume, freshwater (MFT), and heat (MHT) transports through the line using the slow varying geostrophic density field and direct velocity observations. An upper and an abyssal overturning cell are identified with a strength of 15.64 ± 1.39 Sv and 2.4 ± 1.6 Sv, respectively. The net northward MHT is 0.27 ± 0.10 PW, increasing by 0.12 PW when we remove the observed mesoscale eddies with a climatology derived from the Argo floats data set. We attribute this change to an anomalous predominance of cold core eddies during the cruise period. The highest velocities are observed in the western boundary, within the Brazil and the Deep Western Boundary currents. These currents appear as a continuous deep jet located 150 km off the slope squeezed between two cyclonic eddies. The zonal changes in water masses properties and velocity denote the imprint of exchange pathways with both the Southern and the Indian oceans.

Plain Language Summary The Atlantic meridional overturning circulation (AMOC) is a crucial element of the global ocean circulation and climate. It connects the Southern Ocean to the northern North Atlantic, and is responsible for the interhemispheric northward transport of heat and freshwater. The South Atlantic is a crossroad for water masses from the Southern, the Indian and the North Atlantic oceans. This paper analyzes the first full-ocean-depth trans-basin measurements of the southernmost enclosed section of the Atlantic between South Africa and Brazil along 34.5°S. Our results confirm a northward transport of heat at this latitude. We also found a complex water mass structure and dynamics, characterized by intense boundary currents and mesoscale eddies. It is the sum of these elements that is not only crucial for the Atlantic but also for the global ocean circulation and climate.

1. Introduction

The meridional overturning circulation (MOC) is a global-wide circulation pattern that connects the overturning cells confined within ocean basins and helps to promote the balance of the net buoyancy loss in the northern North Atlantic and around Antarctica. While the excess heat from the tropics is transported by the upper ocean to higher latitudes in each basin through the western boundary currents as a response to the wind-driven circulation, the density-driven part of the MOC originates from sinking waters at high latitudes. It consists of two global-scale meridional overturning cells. The "upper-cell," responsible for most of the volume transport; it is linked to the formation of North Atlantic Deep Water (NADW) in the subpolar North Atlantic and Nordic Seas, but also to the upwelling of deep waters in the Southern Ocean. The "lower" or "abyssal" cell is linked to the dense water formation around Antarctica and to the abyssal upwelling due to the interaction of the flow with the bottom topography (Lumpkin & Speer, 2007; T. J. McDougall & Ferrari, 2017; Talley, 2003). The MOC plays a crucial role in the global climate system, with a maximum northward heat transport of 1.3 PW (1.3×10^{15} W) in the subtropical North Atlantic, accounting for 25% of the global combined atmosphere-ocean meridional heat flux (Buckley & Marshall, 2016; Frajka-Williams et al., 2019; Hsiung, 1985; Johns et al., 2011; Talley, 2003).

As the Atlantic Ocean plays a key role in the global system, that segment of the MOC is usually referred to as the Atlantic meridional overturning circulation (AMOC; e.g., Talley, 2003). The South Atlantic is the only basin with a net heat transport from the pole to the equator as the upper 1200 m layer flows northward to compensate for the southward export of colder NADW (Buckley & Marshall, 2016; S. L. Garzoli et al., 2013). Another distinguishing characteristic of the AMOC in the North and South Atlantic is a large disparity in the strength of the abyssal overturning cell between hemispheres. While the abyssal cell transport is roughly 45% the size of the transport associated with upper overturning cell at 34.5°S in the Southwestern Atlantic (7.8 Sv vs. 17.3 Sv respectively; 1 Sv = 10^6 m^3 s^{-1}; Kersalé et al., 2020), in the North Atlantic at 26.5°N the abyssal cell is very weak, only about 1 Sv (Frajka-Williams et al., 2011; Lumpkin & Speer, 2007).

The South Atlantic basin exhibits a wide range of interoceanic convergences and mixing of different waters in the upper limb of the upper overturning cell. The landmass configuration in conjunction with the wind-driven circulation leads to an inflow of cold and fresh waters from the Pacific through the Drake Passage via the so-called "cold water route" as well as warmer and saltier Indian Ocean waters via the Agulhas Current leakage around South Africa, which is usually referred to as the "warm water route" (A. L. Gordon, 1985; Rintoul, 1991; Speich et al., 2007, 2001). Large anticyclonic eddies, referred to as Agulhas Rings (Lutjeharms & Gordon, 1987; Ou et al., 1986), filaments, and coastal jets (Lutjeharms et al., 1992) also play roles in the Indian to Atlantic transfer.

The transport of water from the Indian and South Pacific oceans into the South Atlantic has substantial implications for the overturning circulation of the Atlantic Ocean as a whole (A. L. Gordon, 1985). Weijer et al. (1999) and Biastoch et al. (2008) have demonstrated that these interbasin fluxes of heat and salt are important for maintaining the stability of the AMOC. Moreover, coupled general circulation models show a strong sensitivity in the response of the AMOC to the magnitude and direction of the salt transport through the southern boundary of the Atlantic basin (e.g., Cimatoribus et al., 2012; Drijfhout et al., 2011).

Agulhas Rings play a fundamental role in the transport of warm and salty Indian water into the South Atlantic. Recent studies have shown these eddies have a particularly long lifetime, which can exceed 4 years, and that they can cross the South Atlantic basin and reach the Brazilian coast (Arhan et al., 1999; Guerra et al., 2018; Laxenaire et al., 2018). As they move in the South Atlantic, the core water masses are modified by local air-sea interactions (S. L. Garzoli & Matano, 2011; Laxenaire et al., 2019). This complex circulation within the South Atlantic represents a strong motivation to study the AMOC in the South Atlantic.

Broader understanding of the importance of AMOC variability in the South Atlantic led to the development of an international initiative to study the AMOC in the South Atlantic—the South Atlantic meridional overturning circulation initiative (SAMOC; e.g., Ansorge et al., 2014; Speich et al., 2009). Over the last few decades, several efforts have been made to measure the AMOC strength in the South Atlantic. Snapshot trans-basin ship sections were conducted as part of the World Ocean Circulation Experiment (WOCE) in the 1980s and 1990s, and some of these sections were later repeated as part of the Global Ocean Ship-based Hydrographic Investigation Program (GO-SHIP; e.g., Sloyan et al., 2019; Talley et al., 2016). These sections

Table 1
Summary of Previous Estimates of South Atlantic Upper Overturning Circulation ($AMOC_{max}$), Total Meridional Heat (MHT) and Freshwater Transport (MFT), at 34.5°S and Nearby Latitudes

Source	Section-latitude	$AMOC_{max}$ (Sv)	MHT (PW)	MFT (Sv)	Date (mm/yy)	Data
Hernández-Guerra et al. (2019)	A10-30°S	11.7–17.7	Not provided	Not provided	11/03–9/11	GO-SHIP
Bryden et al. (2011)	24°S	21.5–16.5	0.7–0.4	0.04–0.17	2/83–2/09	GO-SHIP
McDonagh and King (2005)	A10-30°S	Not provided	0.22 ± 0.08	0.5 ± 0.1	12/92	GO-SHIP
McDonagh and King (2005)	A11-45°S	Not provided	0.43 ± 0.08	0.7 ± 0.1	12/92	GO-SHIP
Holfort and Siedler (2001)	A10-30°S	Not provided	0.29	Not provided	12/92	GO-SHIP
Holfort and Siedler (2001)	A11-45°S	Not provided	0.37	Not provided	12/92	GO-SHIP
S. L. Garzoli et al. (2013)	AX18–35.1°S	18.1 ± 2.3	0.54 ± 0.14	Not provided	02–11	XBTs, Argo and WOD
Majumder et al. (2016)	34.5°S	20.66 ± 4.13	0.66 ± 0.21	Not provided	00–14	Argo & Altimetry
Dong et al. (2015)	34.5°S	19.5 ± 3.48	0.49 ± 0.22	Not provided	93–06	Altimetry
Kersalé et al. (2020)	34.5°S	17.3 ± 5.0	Not provided	Not provided	09/13–07/17	PIES
C. S. Meinen et al. (2018)	34.5°S	14.7 ± 8.3	Not provided	Not provided	03/09 12/10	CPIES & model
Perez et al. (2011)	34.5°S	15.6 ± 3.1	0.42+-0.18	Not provided	86–98	Model

Note. The reference citation, date, and data used are also shown. Note that different studies used different error estimate methods.

are surveyed with high accuracy, full depth, coast to coast measurements with a spatial resolution of near the internal Rossby deformation radius (around 40 km for the deep ocean at 34.5°S; Talley et al., 2016). The data provide a quasi-synoptic picture of an oceanic section, although conducting a trans-basin section/cruise at these latitudes takes roughly a month. Assuming the ocean to be in hydrostatic and geostrophic balance, the meridional flow can be estimated considering boundary conditions such as a mass balance (Wunsch, 1996). At least four GO-SHIP sections along the A10 transect nominally along 30°S have been conducted since 1993 (e.g., Hernández-Guerra et al., 2019). Likewise, another four GO-SHIP sections have been occupied along 24°S (e.g., Bryden et al., 2011) and one along 45°S (Holfort & Siedler, 2001) over the same time period.

Repeated eXpendable BathyThermograph (XBT) transects collected via ships of opportunity have also been used to estimate quasi-quarterly meridional transports of volume and heat over the past 2 decades; XBT probes measure the temperature in the upper 800 m or so, with these data being combined with data from deeper reaching profile data (e.g., Argo profiles), with satellite altimetry data, and/or with deep ocean historical climatologies in order to calculate AMOC and MHT (Dong et al., 2009, 2015; Garzoli & Baringer, 2007; S. L. Garzoli et al., 2013; Majumder et al., 2016). A summary of historical oceanic flux calculations from GO-SHIP sections and XBTs transects in the South Atlantic are shown in (Table 1).

Another approach to measuring the AMOC is via basin-wide arrays. These arrays typically involve a mix of geostrophic/density end point moorings and direct velocity observing systems, such as the RAPID-MOCHA-WBTS array deployed at 26.5°N (e.g., Cunningham et al., 2007) and the OSNAP array within the Subpolar North Atlantic (Lozier et al., 2017). Using auxiliary data (e.g., hydrographic information for the interior ocean) additional properties such as the MHT can be estimated from these trans-basin arrays as well (e.g., Johns et al., 2011). The arrays provide high resolution (daily) observations and a key finding has been that the AMOC transport shows surprisingly large variability on intraseasonal to interannual timescales (e.g., Cunningham et al., 2007; Kanzow et al., 2010; Lozier et al., 2019; Srokosz & Bryden, 2015).

Basin-wide AMOC arrays in the South Atlantic include the international South Atlantic MOC Basin-wide Array (SAMBA; e.g., Ansorge et al., 2014; Speich et al., 2009) at 34.5°S and an array at 11°S (e.g., Herrford et al., 2020). The SAMBA line of moorings began in a pilot mode in 2009, with a much better resolved array put in place beginning in 2013. SAMBA consists primarily of pressure-equipped inverted echo sounders (PIES) and current-and-pressure-equipped inverted echo sounders (CPIES), with four additional tall dynamic height/current meter moorings added on the South African continental margin in 2014 (e.g., Kersalé et al., 2018, 2020, 2019; C. S. Meinen et al., 2013; 2018). Hydrographic observations collected during the

mooring maintenance cruises provide regional snapshots of the flow patterns and water mass regimes in the boundary regions. For example, the location and strength of two branches of the lower limb of the AMOC at 34.5°S, each carrying significant flows of recently ventilated North Atlantic Deep Water, have been identified using shipboard hydrographic observations as well as moored observations on both the western (e.g., Valla et al., 2018, 2019) and eastern boundaries (e.g., Kersalé et al., 2018, 2019).

The strength of the AMOC (henceforth referred to as $AMOC_{max}$) at each latitude is defined as the vertical maximum of the stream function and is always located in the upper-cell (Buckley & Marshall, 2016). Different observational estimates of the $AMOC_{max}$ at 34.5°S or in close proximity vary from 17.9 Sv to 18.1 Sv (XBTs; Dong et al., 2009; S. L. Garzoli et al., 2013), 11.7–21.5 Sv (trans-basin hydrographic cruises; Hernández-Guerra et al., 2019), and 19.5–20.7 Sv (Argo- and satellite-derived MOC; Majumder et al., 2016). Using the shallowest PIES mooring at each margin of the SAMBA section together with Ekman transport estimates from gridded observation-based winds (Cross-Calibrated Multi-Platform) and a time-mean reference velocity estimate at one specific depth from different ocean models, the $AMOC_{max}$ upper-cell transport over a period of $\sim$ 6 years has been estimated to be about 14.7 $\pm$ 8.3 Sv (temporal standard deviation; C. S. Meinen et al., 2018). More recently, estimates that include the full array of SAMBA PIES and CPIES between September 2013 and July 2017 provide an $AMOC_{max}$ time-mean upper-cell transport value of 17.3 Sv and a temporal standard deviation of 13 Sv after applying a 30-day low-pass filter (Kersalé et al., 2020). Kersalé et al. (2020) also estimated a time-mean value of 7.8 $\pm$ 6.2 Sv transport of the $AMOC_{max}$ abyssal-cell.

It should be noted that estimates like the latter in the South Atlantic are far fewer in number, coming solely from hydrographic sections between latitudes ranging from 24°S to 32°S. It should also be noted that the methods applied to the SAMBA mooring array rely on a time-mean reference velocity from numerical models at one specific depth. In addition, as no measurements exist inshore of 1,350 dbar on both boundaries, estimates in those shelf areas are also based on model velocities. As such, only the variability of $AMOC_{max}$ from the SAMBA PIES/CPIES array is a complete robust observational assessment (Kersalé et al., 2020).

Previous estimates of the $AMOC_{max}$ variability at this latitude from blended altimetry and XBT sections data (e.g., Dong et al., 2015) or Argo float data (e.g., Majumder et al., 2016) have revealed substantial seasonal to interannual variability, where the Ekman as well as the geostrophic transport contribution play a role both showing annual cycles, which are out of phase. The SAMBA-SAMOC observations have also demonstrated a significant high-frequency variability (Kersalé et al., 2020; C. S. Meinen et al., 2018). Both baroclinic (density) and barotropic (bottom pressure) variations at the eastern boundary at 34.5°S show significant or even dominant contributions to the overall AMOC variability at 34.5°S. These findings are different to the ones at 26.5°N, where previous work has shown that the baroclinic (density) component in the eastern boundary contributes primarily on the seasonal time scale (e.g., Chidichimo et al., 2010). At interannual time scales, large ($\sim$3 Sv) changes in the $AMOC_{max}$ have been observed both at 26.5°N and 34.5°S (e.g., C. S. Meinen et al., 2018; Smeed et al., 2018). A recent study which used the entire SAMBA moored array has shown that the amplitude of the $AMOC_{max}$ variability at 34.5°S is even larger than previously estimated with a standard deviation of 15.5 Sv for the upper-cell and 6.2 Sv for the abyssal-cell (Kersalé et al., 2020). The strongest variability occurs on timescales between 30 and 90 days tightly linked to the passage of eddies across the section (Kersalé et al., 2019). At the boundaries, not only the upper layers but also the deep and abyssal flows are highly variable with the standard deviation exceeding the time mean C. S. Meinen et al., 2017; Kersalé et al., 2019; Valla et al., 2019).

In addition to the volume transport, the meridional heat (MHT) and freshwater (MFT) transports associated with the $AMOC_{max}$ are of interest (Table 1), as variations in these flows can have significant impacts on the global climate system (e.g., Lopez et al., 2016). While the $AMOC_{max}$ is logically broken up into upper and abyssal cells, which seem to vary independently (Kersalé et al., 2020), the MHT and MFT estimates are really only meaningful as full-depth calculations. Full-depth MFT have been estimated for latitudes neighboring 34.5°S (Bryden et al., 2011; McDonagh & King, 2005). At 34.5°S MFT estimates have derived combining upper ocean measurements from XBTs and Argo floats merged with deep hydrographic climatologies (Dong et al., 2015; S. L. Garzoli et al., 2013; Majumber et al., 2016) or by analysis of model simulations (Perez et al., 2011; Table 1).

A first set of full-depth trans-basin hydrographic observations along 34.5°S were collected in early 2017 (Figure 1). Here we present the observed hydrographic structure, the derived volume transport or $AMOC_{max}$,

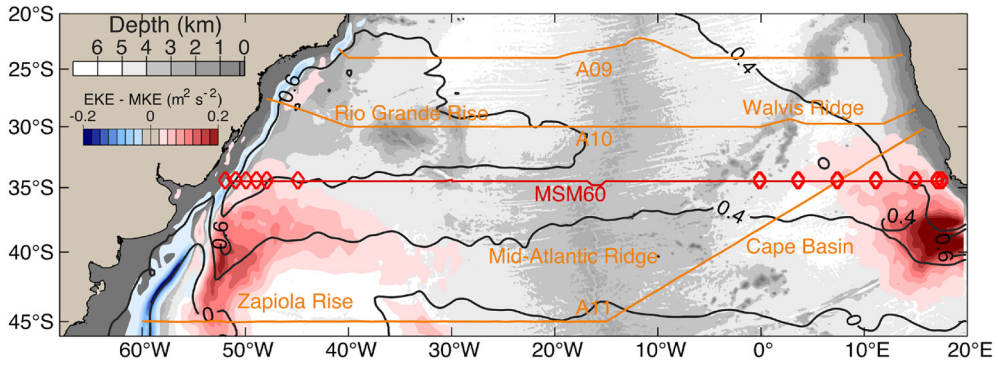

Figure 1. South Atlantic region with the bathymetry from ETOPO2 (Smith & Sandwell, 1997) shaded in gray. In red and blue shades is shown the long-term eddy kinetic energy (EKE) -mean kinetic energy (MKE) computed from Duacs/AVISO surface geostrophic velocity fields. The long-term mean dynamic topography also from Duacs/AVISO is shown as black contours to depict the mean basin circulation. The major bathymetric features are labeled in orange text. GO-SHIP sections are shown as orange lines and the MSM60 cruise track in red. Red diamonds over 34.5°S line show the location of moorings deployed (taken from C. S. Meinen et al., 2017; Kersalé et al., 2019).

MHT, and MFT and compare the results with other estimates, including those from the moored instruments in SAMBA. Moreover, the variability linked to the presence of eddies and its impact on oceanic fluxes along the section is also analyzed.

2. Data

2.1. Ship Observations

We used the hydrographic data collected during the expedition of the German Research Vessel *Maria S. Merian* conducted on January 4 to 31, 2017 (MSM60). In total, 128 full water depth stations (down to 5,450 m) were carried out. These stations were located nominally every 50 km with an increase in horizontal resolution over the continental margins. The rosette system included a pumped Sea-Bird SBE 9plus conductivity-temperature-depth (CTD) system, equipped with double sensor packages for temperature, conductivity (salinity) and oxygen, and lowered acoustic doppler current profilers (LADCP; two Teledyne 300 kHz instruments), and 22 sampling bottles with 10 liter capacity. Water samples were collected for oxygen, salinity, and other chemical properties. Salinity samples were analyzed with Optimare salinometer, Oxygen samples were analyzed on board using the Winkler method, and both were used to calibrate the observations from the CTD. The sampling and calibration for the data reported here followed the respective GO-SHIP recommendations (Hood et al., 2010; Sloyan et al., 2019). Underway measurements included two ship-mounted acoustic doppler current profilers (SADCPs) of 75 and 38 kHz. See further details on the data collection and quality control in Karstensen et al. (2019).

Moreover, ship observations from GO-SHIP sections A09 at 24°S (King & Hamersley, 2010) and A10 at 30°S (M. Baringer & Macdonald, 2013) are used for reference. The data was obtained from the CLIVAR and Carbon Hydrographic Data Office websites. We will applied the same analysis (described in Section 3) to all hydrographic data in order to compare the differences of the AMOC at different latitudes under the same assumptions.

2.2. Satellite Observations

For the analysis the following three satellite data sets were used: (1) 6-h multi-sensor blended winds with a 0.25° horizontal resolution (Bentamy & Fillon, 2012) distributed by the Copernicus Marine Environment Monitoring Service (CMEMS); (2) daily sea surface temperature (SST) at 1 km horizontal resolution from the Group for High Resolution Sea Surface Temperature with its product version four Multiscale Ultrahigh Resolution L4 analysis (Chin et al., 2017); (3) daily Ssalto/Duacs Multimission Altimeter derived absolute dynamic topography (ADT) and derived surface geostrophic velocity fields at a 0.25° horizontal grid and distributed by CMEMS. This data set considers all data recorded by the 12 available altimetric missions

(Duacs/AVISO+, 2015). Note, in the updated version released in April 2014, improved data processing provides a better description of mesoscale activity than previously distributed products (Capet et al., 2014; Pujol et al., 2016).

2.3. Eddy Detection and Colocalized Argo Profiles

The Duacs/AVISO+ (2015) altimetry data set is used as input for the ocean eddy detection and tracking algorithm (TOEddies) and derived database developed by Laxenaire et al. (2018). The TOEddies algorithm is a two-step process: it identifies the occurrences of eddies before deriving their trajectories under the assumption that mesoscale eddies satisfy the geostrophic balance and therefore, enclosed streamlines of ADT should coincide with the location of a mesoscale eddy. The novelty of this algorithm is that it defines and tracks eddies from ADT fields (and not from the sea level anomalies or derived geostrophic velocities) and it considers the complex network of trajectories arising from eddy splitting and merging. A detailed description of the TOEddies can be found in Laxenaire et al. (2018). The TOEddies database is used here for the detection of the mesoscale eddies crossed during the cruise and for the derivation of their trajectories.

The TOEddies database also provides Argo profiles (Argo, 2020) colocalized with eddies and categorized as being "outside" or "inside" anticyclonic (AEs) or cyclonic eddies (CEs). Using this database, we built a summer climatology of the upper 1700 dbar from 648 Argo profiles in close proximity to the 34.5°S section (between 33.5°S and 35.5°S). We used that climatology to substitute the temperature and salinity MSM60 cruise data in the upper 1700 dbar in order to estimate the impact of mesoscale eddies on the AMOC volume, heat and freshwater transport during the cruise. Another climatology was created with TOEddies, in this case to evaluate the expected proportion of AEs and CEs at 34.5°S and the deviations from the mean conditions during the MSM60 cruise. To do so, a daily presence/absence matrix for eddies was created using the entire TOEddies atlas time span (1993–2018) for each longitude grid point at 34.375°S which is one of the closest latitude grid point to the cruise track (the same pattern was observed at 34.625°S). From the matrix, for each grid point of the section, the average monthly percentage of time occupied by an eddy was calculated.

3. Methods

3.1. Data Gridding and Derived Variables

In order to combine the SADCP data (upper 1000 m) with the CTD and LADCP data, the latter was linearly interpolated to an equidistant grid of 1 dbar/0.05 longitude (approximately 4.6 km) between 58°W and 18°E. Given the high-resolution velocity sampling from the SADCP a change in the velocity fine structure occurs at 1,000 m depth because below only discrete LADCP casts are available. A land/bottom mask was created from the ship multibeam echosounder (EM122) data. This approach enabled us to use all measurements while minimizing the impact of bottom triangles (Figure S1).

For all calculations, we used the Gibbs-SeaWater Oceanographic Toolbox containing the thermodynamic equation of seawater 2010 (TEOS-10) subroutines (T. J. McDougall & Barker, 2011). We computed absolute salinity (S_A) and conservative temperature (Θ) from the CTD pressure, temperature and salinity to obtain better estimations of the transport in the South Atlantic Ocean, as the differences of total AMOC transport can reach to 6% when compared with estimates derived from the previous definition of the thermodynamic equation of seawater (Almeida et al., 2018). However, to obtain the neutral density (γ^n) field we also determined potential temperature (θ) and practical salinity (S_p) because currently γ^n is not available as a function of Θ and S_A in TEOS-10 (T. J. McDougall & Barker, 2011; see Figure S2 for differences between Θ and θ and between S_A and S_p along the section). We also derived a composite of daily satellite data for SST and ADT as the ship progressed westward.

3.2. Calculation of the Total Velocity Field: Volume, Heat and Freshwater Transport

Given the large high-frequency variability of the ocean currents observed at 34.5°S (Kersalé et al., 2020; C. S. Meinen et al., 2018) and the non-synoptic nature of the ship survey, we used two approaches to estimate the total velocity field. First, we assumed the combined LADCP and SADCP field (Method 1). Second, from the CTD measurements and following the methodology of Bryden and Imawaki (2001), we used the slow

varying density field to compute the time-averaged mean geostrophic circulation adding also Ekman fluxes. Following M. O. Baringer & Garzoli (2007), Buckley and Marshall (2016) and Holliday et al. (2018), the total meridional velocity field (v) is composed of:

$$v = v_{\text{ageos}} + v_{\text{geos}} + v_{\text{ref}}, \tag{1}$$

where v_{ageos} is the Ekman velocity, v_{geos} the geostrophic velocity, and v_{ref} the barotropic flow.

The zonal integral of v_{ageos} is the Ekman transport calculated as:

$$T_{\text{ek}} = -\int_{x\text{West}}^{x\text{East}} \frac{\tau_x}{f\rho}\,\mathrm{d}x, \tag{2}$$

where τ_x is the zonal component of the local wind stress, f is the Coriolis parameter, and ρ is the density of seawater. To compute the oceanic fluxes, we assumed that the Ekman transport is confined and equally distributed in the top 50 dbar of the water column.

The geostrophic velocity (v_{geos}) was estimated from the hydrography and selecting a certain reference level of no-motion but also explicitly adding a barotropic velocity (v_{ref}). The total meridional velocity field is of central importance for all further calculations and therefore different approaches to estimate the level of no motion and the barotropic velocity were applied to quantify the uncertainties. Note, the uncertainties range given in Section 4 are estimated by applying the different approaches outlined below.

Most importantly we used different levels of no-motion following previous studies. The first two levels of no-motion chosen were the neutral density surface $\gamma^n = 28.10$ kg m^{-3} (Method 2) and 3,400 dbar (Method 3), which is the mean pressure level of the $\gamma^n = 28.10$ kg m^{-3}. This choice was motivated by earlier studies which identified that level as the interface between southward flowing NADW and northward flowing Lower Circumpolar Deep Water (LCDW; e.g., Hernandez- Guerra & Talley, 2016; Hernández-Guerra et al., 2019; McDonagh & King, 2005). For these two methods, we derived a zero net mass transport through the section with a simple barotropic adjustment by adding a small barotropic meridional velocity across the entire section (e.g., M. O. Baringer & Garzoli, 2007).

The third geostrophic approach (Method 4) was to assume the level of no motion at the bottom and then adjust the velocities by adding the near-bottom (within 20 dbar of the bottom) LADCP measurements (e.g., McDonagh et al., 2010). This approach was motivated by the fact that close to the seafloor the LADCP bottom-track mode provides accurate near-bottom absolute velocities (Visbeck, 2002). Again, a small barotropic meridional velocity across the entire section was added to achieve the mass balance. Then, the error estimate from the geostrophic field was computed as the standard deviation of the oceanic fluxes derived from the mass balance total velocity field (v) using the three levels of no motion ($\gamma^n = 28.10$ kg m^{-3}, 3,400 dbar, and bottom).

Not surprisingly, the meridional transport calculations were sensitive to the method used for computing the total velocity field, as shown in the results section. However, the selection of $\gamma^n = 28.10$ kg m^{-3} and equally distributing the mass imbalance as a velocity correction across the section (Method 2) gave a solution that allowed to compare with previous assessments using a similar approach in the South Atlantic, in particular A09 and A10 (Dong et al., 2009; Ganachaud & Wunsch, 2003; S. L. Garzoli et al., 2013; Hernández-Guerra et al., 2019; McDonagh & King, 2005).

A sensitivity analysis was also performed to quantify the effect of mesoscale eddies in the transports and AMOC_{max}. To do so, we replaced the upper 1,700 dbars hydrography with a summer (December-January-February) climatology constructed from the 648 non-eddy Argo profiles available between 33.5°S and 35.5°S based on the TOEddies database (Method 5).

Another common approach to estimate the volume transport across coast to coast trans-basin sections is to use inverse methods. These methods use mass conservation for every vertical layer after predefining several constraints like boundary currents, mean transport and flow through deep channels (Wunsch, 1996). Hernández-Guerra et al. (2019) demonstrated that inversions at 30°S using different models and constraints can lead to very diverse solutions. In this first realization of a GO-SHIP section along the SAMBA line, we choose to assess the transport by a simpler direct approach.

After securing the conservation of mass condition through the section, we obtained the $AMOC_{max}$, MHT, and MFT following Buckley and Marshall (2016) and are expressed in units of Sv, PW, and Sv, respectively. First, we defined a stream function for the zonally integrated meridional volume transport in pressure coordinates:

$$\Psi(y,z) = \int_{x\mathrm{West}}^{x\mathrm{East}} \int_{p\mathrm{max}}^{p\mathrm{min}} v \, \mathrm{d}x\mathrm{d}p, \tag{3}$$

where v is the estimated total meridional velocity component field (see above), x and p are the coordinates in the zonal and vertical domain. Then, we determined the AMOC strength ($AMOC_{max}$) of the upper cell by the maximum value and depth of the stream function over the water column. On the other hand, the $AMOC_{max}$ of the abyssal cell was computed as the net volume transport of AABW.

The meridional heat transport (MHT), was computed as:

$$\mathrm{MHT} = \mathrm{Cp}\rho_0 \int_{x\mathrm{West}}^{x\mathrm{East}} \int_{p\mathrm{max}}^{p\mathrm{min}} v\Theta \, \mathrm{d}x\mathrm{d}p, \tag{4}$$

with Θ the conservative temperature, ρ_0 the section mean potential density and Cp a reference value for the heat capacity of seawater = 3850 J kg^{-1} C^{-1}. Finally, the freshwater transport (MFT) was calculated as:

$$\mathrm{MFT} = \int_{x\mathrm{West}}^{x\mathrm{East}} \int_{p\mathrm{max}}^{p\mathrm{min}} v\left(1 - \frac{S_A}{S_0}\right) \mathrm{d}x\mathrm{d}p, \tag{5}$$

where S_A is absolute salinity and S_0 is the section-averaged absolute salinity. The MFT is approximately $-S_0$ times the salinity transport, with exact equality holding if there is no net mass transport across the section. While the $AMOC_{max}$ used here reflects the intensity of the upper meridional overturning cell only, both MHT and MFT are an estimate of the full-depth oceanic fluxes.

4. Results

4.1. Surface Conditions and Direct Velocity Measurements

The MSM60 underway measurements of SST from the Thermosalinograph (TSG) are in good agreement with satellite observations despite the fact that the TSG temperature sensor is located at 5 m depth (Figure 2a). During the cruise, SST varied from 18.65°C to 25.17°C, increasing westward as expected from both, the climatology and the fact that the cruise was conducted over one month in early austral summer (January) and were we expect SST to increase. From satellite SST data we found that within the area between 25°W and 55°W an increase of SST by up to 4°C is seen (not shown here).

The velocity fields derived from the ADCPs were intense (>0.5 m s^{-1}) in the Brazil Current (BC henceforth) near 50°W and during the crossing of mesoscale eddies. MSM60 crossed 13 cyclonic (named C1–C13, Figures 2a) and 12 anticyclonic (A1–A12, Figure 2a) mesoscale eddies, although not all were crossed at their center as revealed in comparison with the TOEddies database. From the 128 CTD profiles taken during the cruise, 27 (21%) were located within cyclonic eddies and 12 (9%) within anticyclonic eddies. This represents an anomalous predominance of cyclonic eddies (CEs) over anticyclonic eddies (AEs) at the time of the cruise. By analyzing the 26 years of TOEddies database, both the annual and summer means display an expected 19% and 14% of the section occupied with AEs and CEs, respectively. During the month of the cruise in January 2017, the mean percentage of the section occupied by eddies was 14% for AEs and 21% for CEs, locating January 2017 in the 96th percentile in the proportion of CEs with respect to AEs for the 312 analyzed months.

Four long-lived Agulhas rings (A1, A2, A3, and A12) were crossed but only one (A3) was intercepted close to its core and sampled with CTD profiles. A12, was a long-lived Agulhas ring more than 4 years old that crossed the entire basin (Figure S3). The SADCPs also documented two large cyclonic eddies, one centered at 14 °E in the Cape Basin (C1) and another one in the west just east of the BC at 47.4 °W (C12). The

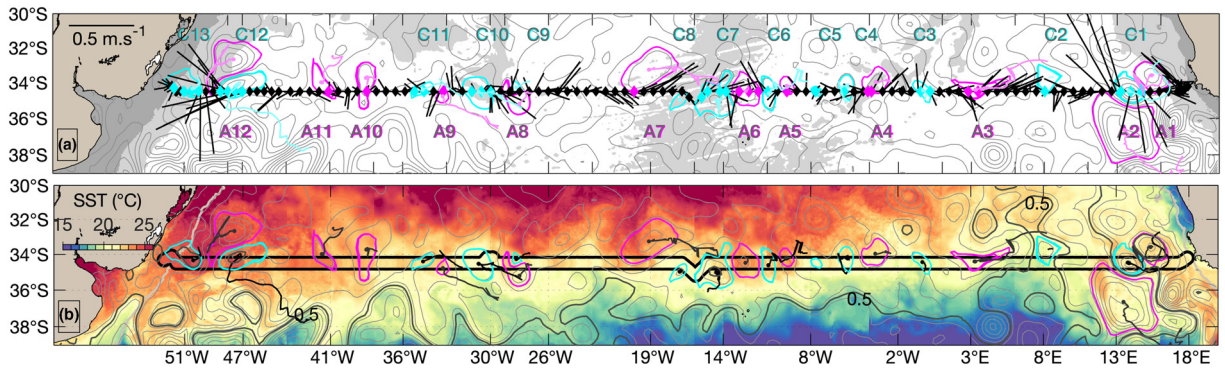

Figure 2. Maps of the South Atlantic with the MSM60 cruise track between 4 and 31 January 2017 from Cape Town, South Africa, to Montevideo, Uruguay. (a) Highlighting the averaged velocity in the upper 100 dbar measured by the 38 kHz SADCP (black sticks) and each of the 128 CTD station locations (black diamonds). The anticyclonic and cyclonic eddies crossed, together with the correspondent CTD profile inside those eddies are colored in magenta and cyan, respectively. The eddy "tails" show the eddy trajectories during the preceding 120 days (or less for eddies with shorter lifespan). ADT composite, computed by taking each day of the cruise track cut by longitude is shown in gray contours. The daily progress of the cruise is displayed as one tick corresponding to one day in the x axis of panel (a) corresponding 18°E to the 4th of January. Bathymetry from 0 to 200 m and 200–3,500 m is shaded in dark and light gray, respectively. (b) SST (shaded) and ADT (gray contours) composite. In between the black lines are plotted the MSM60 TSG temperature measurements at 5 m of depth in the same color scale as SST. In magenta and cyan are the contours of the anticyclonic and cyclonic eddies that intercepted the cruise track. The precedent 120 days (or less for eddies with shorter lifespan) trajectory for each eddy is displayed as a black line. ADT, absolute dynamic topography; CTD, conductivity-temperature-depth; SADCP, ship-mounted acoustic doppler current profilers; SST, sea surface temperature; TSG, thermosalinograph.

reconstructed trajectory of C1 showed the eddy originated from an instability along the Benguela upwelling system front (Figure 2). This is also confirmed by the low dissolved oxygen concentration within the eddy (Figure 4c).

On the eastern margin, the Benguela Current appears as a relatively wide and weak equatorward eastern boundary current, but interacting with the intense cyclonic eddy (C1, Figures 2b and 3a). Near 5ºE, an intrusion of surface subantarctic waters has been observed due to the presence of an intense dipole (Kersalé et al., 2018) associated with satellite-derived ADT lower than 0.5 m at 34.5°S (Figure 1). In this area, during the MSM60 cruise, the ADT was particularly low relative to the time-mean ADT, with the 0.5 m contour reaching 32°S (Figure 2b). This same area was up to 2°C colder compared to its surrounding (Figure 2a). Subtropical waters are generally separated from subantarctic waters by the Subtropical Front (STF; Belkin & Gordon, 1996; Orsi et al., 1995). In the South Atlantic, the STF coincides with ADT ranging between 0.4 m and 0.5 m (e.g., Artana et al., 2019). ADTs lower than 0.5 m along the section correspond to cold, fresh, highly oxygenated water of subantarctic origin (Figure 2). This is the case of the vertical structure of the cyclonic eddy C2 that was crossed at 6°E, (Figure 4). The Θ-S_A diagram shows that the properties of the water in the eddy are characteristics of the Subantarctic Zone (SAZ) and they form an intrusion of cold and fresh water between the 26.2 and 26.4 kg m^{-3} isopycnals in comparison with surrounding waters within the same density (Figure 5a). Though the water mass properties clearly point to the subantarctic origin of these waters, it was not possible to track eddy C2 back to the SAZ as its trajectory is short and complex (it is embedded in a subantarctic intrusion where frequent eddy splitting and merging occurs and only short-lived coherent structures are observed). Nevertheless, other long-lived coherent eddies that have intercepted the SAMBA section during the MSM60 cruise originate in the SAZ (e.g., C12). All these eddies are characterized by ADT lower than 0.5 m (Figure 2).

4.2. Water Masses and Layering

For water mass definitions we followed Valla et al., (2019) and Hernández-Guerra et al. (2019) and separated the water column along the SAMBA section in seven main water masses (see Table 2). Surface Water (SW) is considered a layer in constant transformation due to air-sea fluxes and as such cannot be considered as a water mass in a proper sense. SW is defined by $\gamma^n < 26.35$ kg m^{-3}, it has a mean pressure of 70 dbar and includes the upper part of South Atlantic Central Water (SACW). SACW is formed by subduction in the subtropical gyre and extends to about 750 dbar or $\gamma^n = 27.10$ kg m^{-3} which includes the permanent thermocline layer (A. L. Gordon, 1981, 1986). SACW has the largest temperature and salinity range (17–7°C

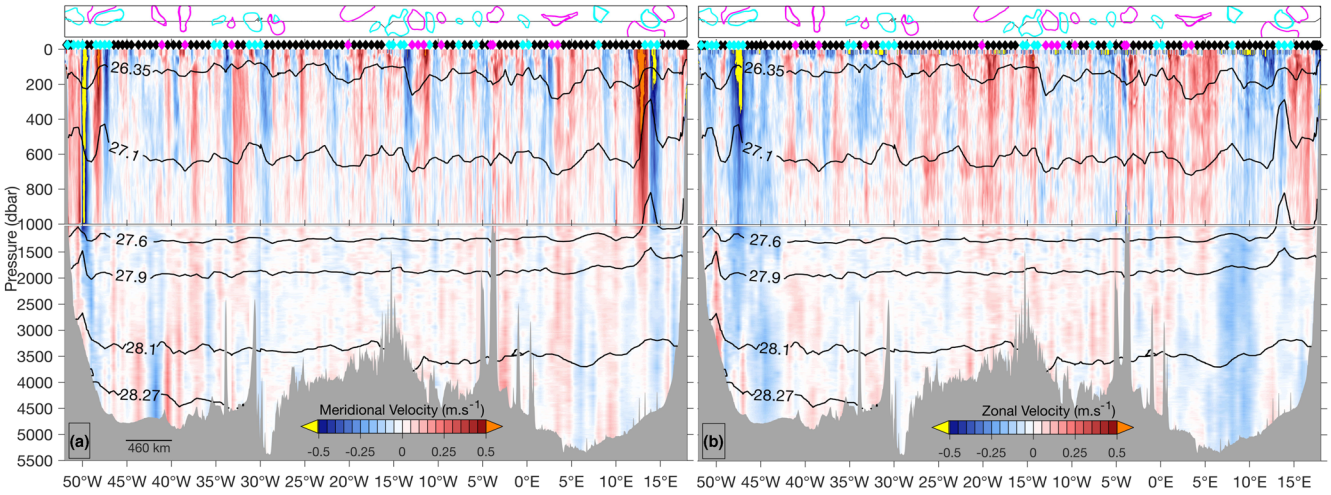

Figure 3. Direct velocity measurements along 34.5°S. The upper 1,000 dbars are vertically stretched and show spatially higher resolution SADCP measurements. The deep velocity section is derived from 128 LADCP profiles. (a) Meridional Velocity (m s^{-1}) and (b) Zonal Velocity (m s^{-1}). Values above 0.5 m s^{-1} and below −0.5 m s^{-1} are colored in orange and yellow for better visualization, respectively. Details inside those areas are shown in Figures 10 and 11. Neutral density layers (γ^n, kg m^{-3}) bounding each water mass are shown in black. LADCP, lowered acoustic doppler current profilers; SADCP, ship-mounted acoustic doppler current profilers.

and 34.6–36.1 g kg^{-1}) leading to a considerable stratification, which is even stronger toward the east of the basin (Figures 4d and 5a).

Below the thermocline, between 750 and 1,140 dbar (27.10 kg m^{-3} < γ^n < 27.58 kg m^{-3}), lies the highly oxygenated, low-salinity (<34.5 g kg^{-1}) Antarctic Intermediate Water AAIW. The AAIW found in the Atlantic Ocean has contrasting properties across the basin (McCarthy et al., 2011; Piola & Georgi, 1982; Rusciano et al., 2012). Atlantic AAIW originates from two different source waters (see Rusciano et al., 2012 for a detailed discussion): Subantarctic Mode Water (SAMW) that is transformed in a fresh variety of AAIW in the southwest South Atlantic (Piola & Gordon, 1989; Suga & Talley, 1995) continuing eastwards along the southern edge of the South Atlantic Current and along the Atlantic portion of the SAF (A-AAIW hereafter, characterized by $S_P \leq 34.2$; $S_A \leq 34.4$; Boebel et al., 1999; McCartney, 1977; Rusciano et al., 2012; Tsuchiya et al., 1994). A-AAIW extends from the western continental slope to 25°W and it is characterized by dissolved oxygen concentration above 250 μmol kg^{-1} (Figure 4c). The other source is AAIW of Indian origin (I-AAIW, $S_P \geq 34.3$; $S_A \geq 34.45$) that enters the South Atlantic through the Agulhas/Benguela Current system (A. L. Gordon et al., 1987; A. L. Gordon et al., 1992; Rusciano et al., 2012; Stramma & England, 1999). I-AAIW lies in the easternmost sector of the section, east of 12°E in the Cape Basin and is characterized by oxygen concentrations lower than 200 μmol kg^{-1}. A third variety is sometimes called Indo-Atlantic AAIW (IA-AAIW, 34.2 < S_P < 34.3; 34.4 < S_A < 34.45), which is created by isopycnal mixing of A-AAIW and I-AAIW in the Cape Basin and covers a depth range of 800–1,000 m depth (Capuano et al., 2018; A. L. Gordon et al., 1987; Rusciano et al., 2012). Consequently IA-AAIW is found between A-AAIW and I-AAIW, from the Mid-Atlantic Ridge to ~12°E (Figures 4c and 5b).

Below the AAIW layer, between 1,140 and 1,600 dbar (27.60 <γ^n <27.90 kg m^{-3}), we observe Upper Circumpolar Deep Waters (UCDW) through a minimum in dissolved oxygen (ca. 180 μmol kg^{-1}). UCDW is more zonally homogenous in terms of thermohaline and oxygen properties from west to east in comparison with AAIW (Figures 4c and 5b). This is probably due to the fact that UCDW enters the western South Atlantic mostly through the Drake Passage (Callahan, 1972) and the South Atlantic Current (Stramma & England, 1999), but despite a small recirculation in the southeast Indian Ocean, there is no major evidence of UCDW sources in the Indian Ocean unlike for AAIW (Stramma & England, 1999).

Between 1,600 and 3,400 dbar (27.90 < γ^n < 28.10 kg m^{-3}) two varieties of NADW are observed (Figure 4). W-NADW is found in the western part of the section. This water mass is more saline (34.9 < S_A < 35.15) and better oxygenated (230 < O2 < 245 μmol kg^{-1}; Figure 4) than the NADW in the eastern part of the section (E-NADW, 34.9< S_A < 35 and 200 < O_2 < 227 μmol kg^{-1}; Arhan et al., 2003). The contrast between the

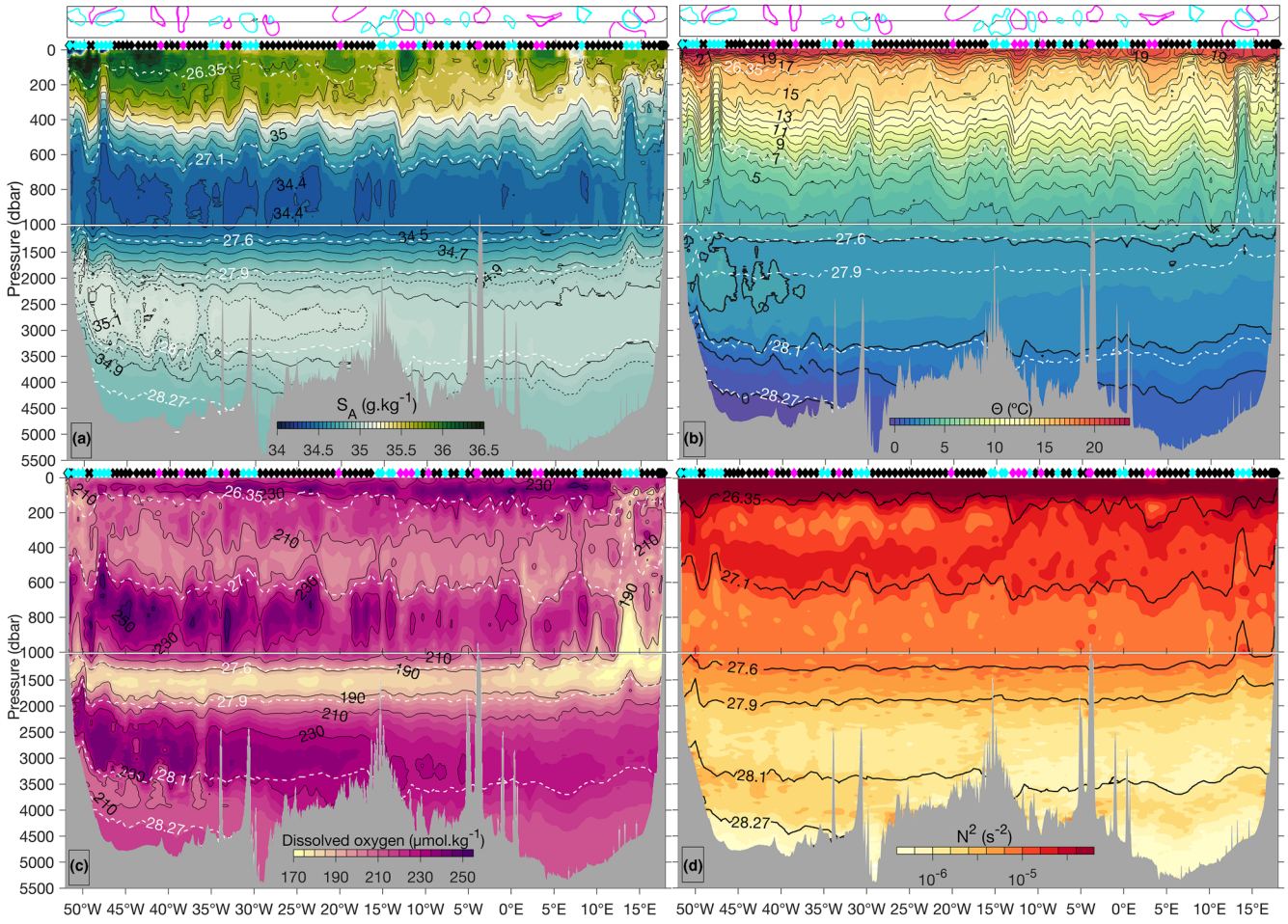

Figure 4. Water properties observed during the MSM60 cruise. (a) Conservative temperature (Θ, (°C), (b) Absolute salinity (S_A (g kg^{-1})), (c) Dissolved oxygen (µmol kg^{-1}), and (d) Brunt–Väisälä frequency (N^2 (s^{-2})). The neutral density layers (γ^n (kg m^{-3})) bounding each water mass are shown in white dotted lines in (a), (b), (c), and in black lines (d), respectively. A map showing the location of anticyclonic and cyclonic eddies crossed during the cruise in magenta and cyan respectively is shown on top of panels a and (b. The diamonds indicate the location of the 128 CTD profiles, colored in black, magenta and cyan depending if they were occupied outside, or within an anticyclonic or a cyclonic eddy, respectively. The upper 1,000 dbars are vertically stretched. CTD, conductivity-temperature-depth.

two NADW blends stems from W-NADW being more directly transported southward by the Deep Western Boundary Current from its formation region in the Labrador Sea and the Greenland-Scotland Ridges system (Reid et al., 1977; Table S1). The core of E-NADW is more difficult to identify, as it is even more eroded, characterized by homogeneous thermohaline properties with respect to its surroundings ($35 < S_A < 35.05$; $34.80 < S_p < 34.85$; $220 < O_2 < 227$ µmol kg^{-1}; Figure 4a). According to Arhan et al., (2003), the E-NADW transport is southward (11 ± 4 Sv) at 35°S and its flow can be traced upstream across the Cape Basin to passages across the Walvis Ridge south of 28°S, and then back to the deep western boundary current of the Atlantic Ocean near the tropics as proposed by Reid (1989).

Along its southward path, NADW penetrates toward the Southern Ocean and transforms into Circumpolar Deep Waters, which in the South Atlantic is split into two layers by the southward flowing NADW: UCDW and Lower Circumpolar Deep Water (LCDW; Lumpkin & Speer, 2007; Reid et al., 1977). LCDW is located below NADW and above Antarctic Bottom Waters (AABW) at $28.1 < \gamma^n < 28.27$ kg m^{-3}. Data from the MSM60 section suggest that the observed LCDW undergoes mixing with NADW and AABW with considerable zonal differences in thermohaline characteristics and flow direction, being the water mass layer that exhibits the largest differences between the western and the eastern sides of the section. Zonal differences in LCDW thermohaline and oxygen properties are observed along the SAMBA line (Figure 5 and S5). The LCDW property diversity coincides with very specific domains separated by the steep topographic features,

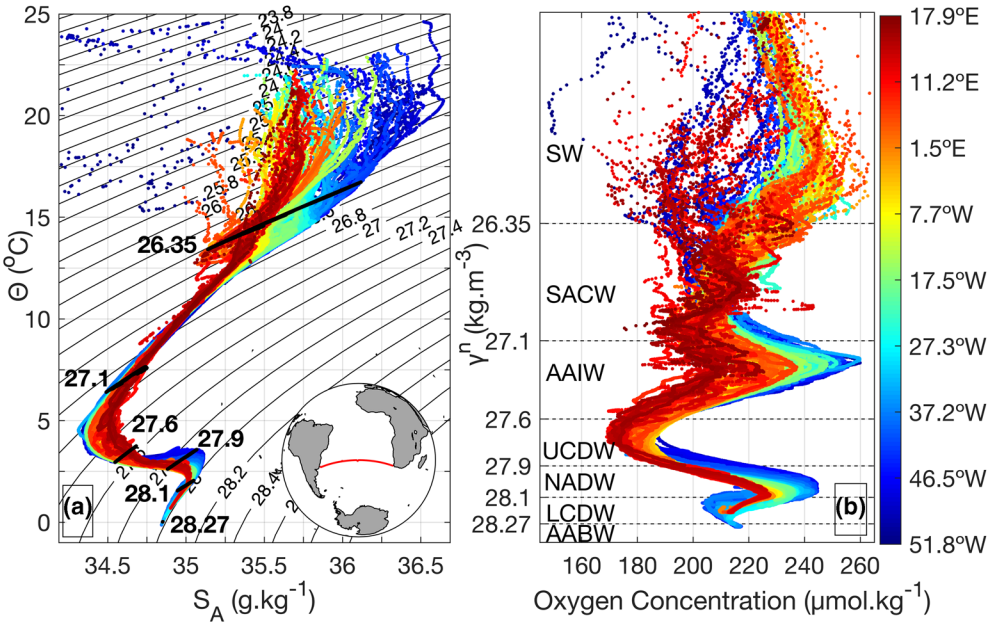

Figure 5. (a) Θ-S_A diagram for the CTD profiles collected during the MSM60 cruise. S_A < 34 g kg^{-1}1 has been clipped for better visualization. Bold black lines and numbers represent the neutral density levels between water masses (shown in b). See Figure S4 for θ-S_P diagram. The cruise track is shown in the insert. (b) Dissolved oxygen concentration (µmol kg^{-1}) as a function of neutral density (kg m^{-3}). Water mass acronyms and selected neutral density boundaries are indicated by dashed lines. For references to the water mass see Table 2. CTD, conductivity-temperature-depth.

such as the Rio Grande Rise at 31°W, the Mid-Atlantic Ridge at 16°W, and Walvis Ridge at 4°W (Figure 1). West of 31°W, W-LCDW is clearly identified as a layer of about 1,000 dbar of thickness lying between 3,000 and 4,000 dbar (Figure 4). There, it flows northward synchronically with AABW, and it differs from the latter mainly in its dissolved oxygen concentration, ranging between 202 and 214 µmol kg^{-1} in W-LCDW and 214–218 µmol kg^{-1} in AABW, respectively (Figures 4c and 7b; Valla et al., 2018). W-LCDW is the less oxygenated variety of LCDW (<214 µmol kg^{-1}) and its properties can be traced back as a mixing between AABW and NADW (Reid, 1989). East of 31°W, the LCDW isopycnal layer, as we have defined it, flows southward and it extends vertically down to the seafloor (Figures 6b and 7b). As there is no AABW east to 30°W, LCDW is mainly influenced by the NADW, with slight differences in thermohaline properties across topographic features. Between the Rio Grande Rise and the Mid Atlantic Ridge, there is still an influence of W-LDCW, with relatively low oxygen, salinity and temperature, especially in the deep channel at 30°W (Figure 4). The warmest, relatively saltiest, and highly oxygenated variety of LCDW is observed between the Mid-Atlantic Ridge and the Walvis Ridge, possibly due to the influence of still relatively pristine NADW. The fact that this portion of the section is shallower than the Cape Basin, topography prevents the flow of the densest (coldest) variety of LCDW. Finally, the most eroded variety of E-LCDW is observed in the Cape Basin, east of 3°W. That water mass presents notably homogeneous thermohaline composition and therefore it is difficult to trace its origin based solely on the thermohaline and dissolved oxygen properties. It has been argued that the origin of E-LCDW can be traced to older (e.g., relatively less salty and oxygenated) varieties of NADW and AABW (Arhan et al., 2003; Gladyshev et al., 2008; Reid, 1989; Stramma & England, 1999).

Finally, in the western basin, younger AABW, the densest and coldest water mass (γ^n > 28.27 kg m^{-3}) extends from 3,420 dbar to the seafloor and at 34.5°S is confined to the Argentine Basin west of 33°W. This water

Table 2
Neutral Density Ranges (γ^n) and Mean Pressure, Conservative Temperature (Θ), Absolute Salinity (S_A), Practical Salinity (S_P), and Oxygen Concentration (µmol kg^{-1}) per Water Mass Across 34.5°S in the Atlantic

Water Mass	γ^n (kg m^{-3})	Pres. (dbar)	Θ (°C)	S_A (g kg^{-1})	S_P (psu)	O_2 (µmol kg^{-1})
SW	<26.35	79	17.85	35.74	35.57	228.13
SACW	26.35–27.10	377	11.63	35.22	35.05	211.34
AAIW	27.10–27.60	921	4.34	34.48	34.31	216.66
UCDW	27.60–27.90	1549	2.88	34.76	34.59	185.59
NADW	27.90–28.10	2,637	2.47	35.02	34.85	223.39
LCDW	28.10–28.27	4,432	1.07	34.92	34.77	216.09
AABW	>28.27	4,544	-0.07	34.85	34.67	215.87

Note. Acronyms correspond to Surface Water (SW), South Atlantic Central Water (SACW), Antarctic Intermediate Water (AAIW), Upper Circumpolar Deep Water (UCDW), North Atlantic Deep Water (NADW), Lower Circumpolar Deep Water (LCDW) and Antarctic Bottom Water (AABW).

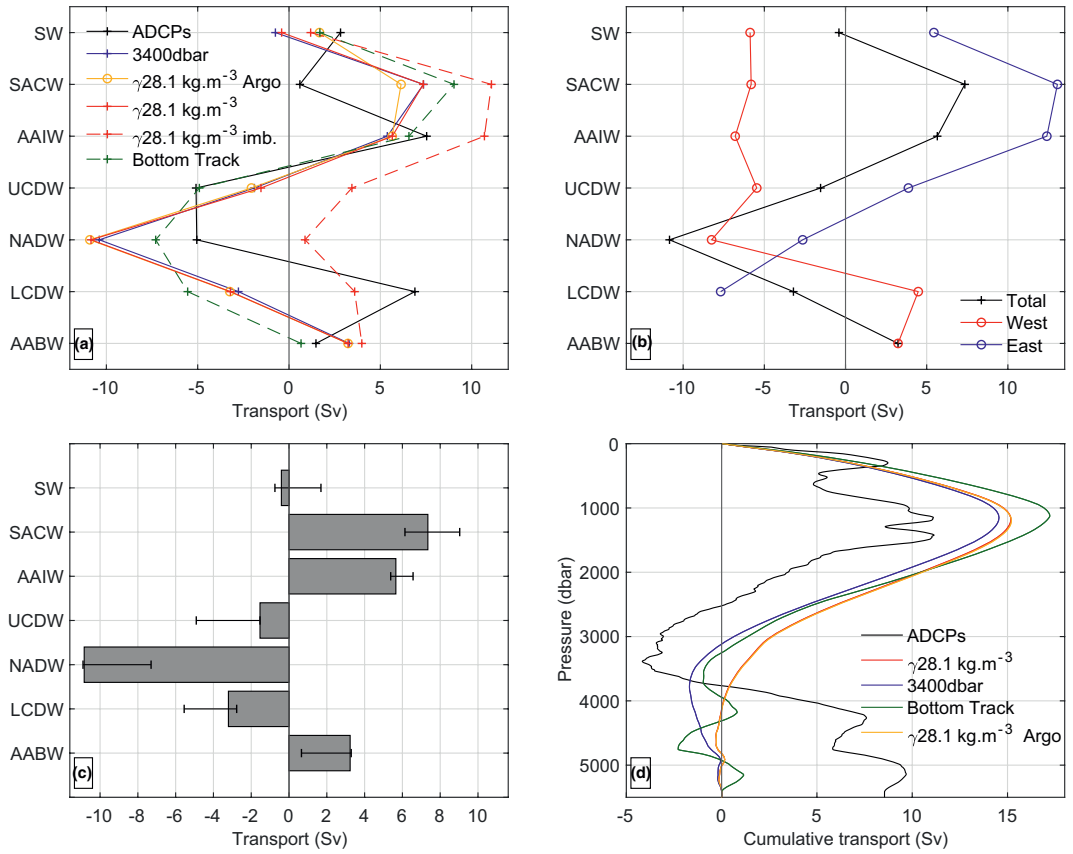

Figure 6. MSM60 meridional volume transport at 34.5°S in the South Atlantic. (a) Transport by isopycnal layers referring to specific water masses. Each color represents a different method: direct observations from ADCPs are shown in black (Method 1), while the rest are based on the geostrophic approaches and are shown in red, blue, green and yellow for Methods 2, 3, 4, and 5, respectively. The dashed red line represents the volume transport estimate obtained with no barotropic adjustment from Method 2. (b) West (red), East (blue) and total (black) transport by water mass from Method 2. The South Atlantic was separated in West and East at 17°W, close to the Mid-Atlantic Ridge. (c) Volume transport by water mass. Gray bars show the calculation from Method 2. The error bars represent the minimum and maximum estimates from all the mass balanced methods used to estimate the total velocity using the original data. (d) Cumulative volume transport by pressure level for the different methods.

mass is formed in the surroundings of Antarctica, mainly in the Weddell Sea (Orsi et al., 1999) and therefore it is highly oxygenated ($O_2 > 225$ μmol kg^{-1}) and characterized by particularly low temperature ($\Theta < 0$°C). The $\gamma = 28.27$ kg m^{-3}, which is commonly used to separate LCDW from AABW, closely follows the 0°C isotherm, also used as the upper bound for AABW (Georgi, 1981; Valla et al., 2019; Figure 4a).

The MSM60 data show that besides the common layering, substantial differences between the western and the eastern basins can be identified (Figure 5, S5,and S6 and Table S1). These differences reflect the contrasting origins and trajectories of water masses converging in the South Atlantic at 34.5°S (A. L. Gordon et al., 1992; Speich et al., 2001; 2007) that ultimately affects the large-scale transport of heat, freshwater and biogeochemical components such as nutrients and carbon.

4.3. Volume, Heat and Freshwater Transports

We estimated an Ekman transport of −0.42 Sv across the entire transect using the satellite wind measurements. The zonally integrated Ekman transport at 34.5°S computed for the period 2009–2018 from satellite data shows a pronounced annual cycle. Austral winter values are the highest, with a maximum of 8.24 Sv in June, due to the equatorward migration of the semi-permanent anticyclone in the atmosphere, whereas

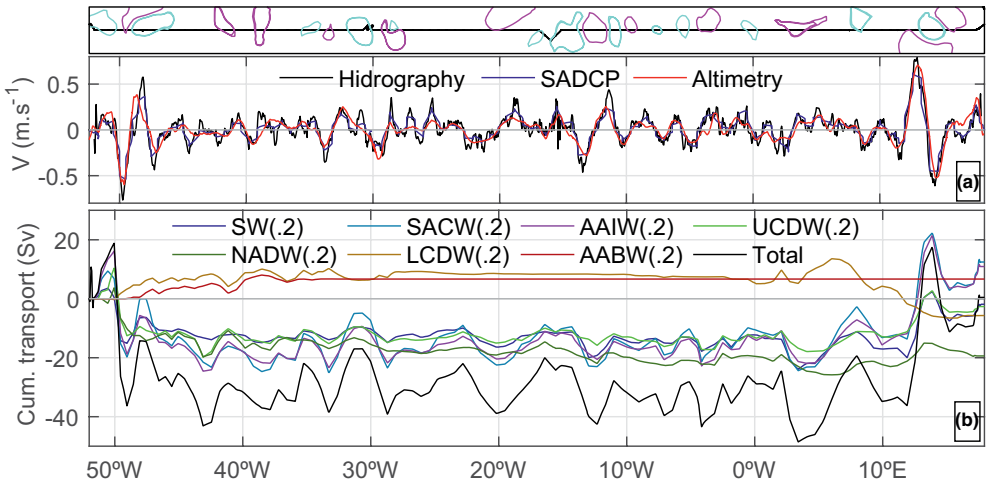

Figure 7. (a) Averaged upper 100 dbar surface velocity derived from hydrography applying the geostrophic equilibrium and mass-balanced adjusted, and SADCP are shown in black and blue, respectively. Surface geostrophic velocities from altimetry are shown in red. (b) Cumulative vertically integrated meridional transport across 34.5°S from west to east. The individual water masses have been multiplied by 2 for better visualization. SADCP, ship-mounted acoustic doppler current profilers.

in austral summer the Ekman transport is the lowest. Hence, the observed Ekman transport during the MSM60 cruise was close to its climatological value for January of 0.27 Sv (Figure S8).

The volume transport from ADCPs measurements (Method 1) generates an initial imbalance of 8.54 Sv, which is not surprising given that it took 28 days to cross the entire section and large transport variability at shorter time scales (15.5 Sv daily standard deviation in the upper cell) revealed from daily trans-basin transport estimates (Kersalé et al., 2020). Another possible source of error may be linked to a too coarse sampling of the narrow and intense western boundary current below 1,000 dbar and where only data at discrete CTD (LADCP) stations is available. Applying Method 2, this initial imbalance increases to 34.64 Sv when we calculate the geostrophic transport relative to a level of no motion at $\gamma^n = 28.10$ kg m^{-3}. As discussed in Section 3.2, transport estimates are particularly sensitive to the choice of such level (Figure 6 and Table 3). However, this level allowed us to compare the results with previous studies in the region (Dong et al., 2009; Ganachaud & Wunsch, 2003; S. L. Garzoli et al., 2013; Hernández-Guerra et al., 2019; McDonagh & King, 2005). In particular, this initial volume transport imbalance is similar to the 36 Sv obtained by Hernández-Guerra et al. (2019) using geostrophic velocities and the same level of no motion at 30°S.

The zonally integrated volume transport shows the two overturning cells expected at this latitude, with an upper cell with northward transport in the SACW and AAIW layers approximately down to 1,300 dbar and deeper southward transport of NADW. That is the cell that usually is referred in the literature as the AMOC

Table 3
Overturning Maximum (AMOC), Meridional Heat Transport (MHT) and Freshwater Transport (MFT) in the South Atlantic at 34.5°S Calculations Using Different Approximations

Method	1	2	3	4	5
Data set	ADCPs	CTDs	CTDs	CTDs	Argo/CTDs
Level of no-motion	-	γ^n28.1	3,400 dbar	Bottom	γ^n28.1
Barotropic adj.	-	Mass balance	Mass balance	LADCP bottom + Mass balance	Mass balance
AMOC (Sv)	11.14	15.18	14.55	17.21	15.20
MHT (PW)	0.26	0.23	0.19	0.38	0.35
MFT (Sv)	0.16	0.21	0.24	0.25	0.10

Note. CTD, conductivity-temperature-depth; LADCP, lowered acoustic doppler current profilers.

or the upper overturning cell in contrast to the abyssal overturning cell (e.g., Kersalé et al., 2020). The upper cell is, in our present climate state, more intense than the abyssal cell (Figure 6a). Between 1,300 dbar and 3,400 dbar, the volume transport is mostly southward and associated with NADW, while below 4,800 dbar it switches to a northward flow associated with AABW. Between 3,400 dbar and 4,800 dbar, within the LCDW, northward transport is observed in the west and southward transport is observed in the east, denoting zonal differences (Figure 7b). Indeed, the only inconsistency found in the transport sign between ADCPs and geostrophy was in the eastern LCDW, where ADCPs displayed a mean northward transport. This water mass has been identified by a specific isopycnal layer. However, as we discussed in the previous sections, the LCDW is indeed present near the western boundary at 34.5°S whereas it consists of modified LCDW through mixing with AABW at the eastern end of the basin. This might explain the variability in the direction of the volume transport in this layer.

The $AMOC_{max}$ amounts to 15.64 ± 1.39 Sv considering the original data and the three levels of no motion with mass balance. The maximum northward transport of the cell is achieved between the surface and 1,156 ± 17 dbar (Figure 6d), with estimates ranging between 14.55 Sv and 17.21 Sv depending on the method and data used to compute the total meridional velocity, and 11.14 Sv for the ADCPs, that is not mass balanced (Table 3). These AMOC transports are lower than previous estimates based on different methods and datasets (S. L. Garzoli et al., 2013; Dong et al., 2009; 2014; Table 1). Nevertheless, the MSM60 based estimates fall within the 17.3 ± 5.0 Sv time mean upper cell transport from Kersalé et al. (2020) using PIES, which also presented a very large peak-to-peak variability in the 2013–2017 period, and a very large transport anomaly (∼-20 Sv) in January 2017 (Figure S7). Overall, the recent studies from moored arrays have suggested that the transport variability across 34.5°S is very high, even within a month. This strong basin-wide variability is mostly caused by fluctuations at the western and eastern boundaries (Kersalé et al., 2020, 2019; C. S. Meinen et al., 2017, 2018).

The MHT estimate during MSM60 is 0.27 ± 0.10 PW when derived from the mass balanced geostrophic approximation using three different levels of no-motion and 0.26 PW using ADCPs data. These values are also lower than the estimates of 0.55 ± 0.14 PW by Dong et al (2009) at 35°S. The low $AMOC_{max}$ and MHT values could be partially explained by the intense (heat) transport observed for the southward flowing BC during the MSM60 cruise and the low $AMOC_{max}$ state reported by Kersalé et al., (2020) for the same period. Moreover, the predominance of cyclonic eddies with large negative temperature anomalies along the section (e.g., C1 and C12) could also explain both the low MHT and the increase of 0.16 PW in MHT when replacing the upper 1,700 dbar with the non-eddy Argo climatology (Table 3). As eddies are not perfectly symmetric and were not crossed at the center, they have a net contribution to the MHT. While the contribution to the MHT between 1,701 dbar and the bottom is −0.17 PW for both datasets (as they are essentially the same), the upper 1,700 dbars contribution to the MHT are 0.40 and 0.55 PW for the original and Argo climatology datasets, respectively. No substantial increase in the $AMOC_{max}$ was observed for the above-mentioned datasets, where eddies under this eulerian approach seem to have a small contribution (Table 3).

Freshwater transport is on average 0.23 ± 0.02 Sv when derived from the mass balanced geostrophic approximation using three different levels of no-motion ranging from 0.10 to 0.25 Sv according to the method and data set used (Table 3).

In order to assess how the volume transport is distributed not only in the vertical but also zonally across the section, we computed the vertically integrated transport and the cumulative sum transport for each water mass across the SAMBA section, from west to east (Figures 6b and 7b). In addition, we compared the averaged upper 100 dbar geostrophic velocity derived from hydrography with Method 2 to SADCP velocity and the surface geostrophic velocity derived from satellite altimetry ADT. They compare well, in terms of spatial variability and amplitude and this gives confidence on in situ velocity estimates (Figure 7a). The vertical integrated transport per longitude across the SAMBA section confirms, as discussed in previous studies (e.g., C. S. Meinen et al., 2018), that the eastern and western boundaries play a dominant role in setting the AMOC. The western boundary shows a northward flow from the shelf to the mid-slope at 50 ºW, and then an intense southward flow associated with both, the BC and the Deep Western Boundary current. On the other hand, the eastern boundary is characterized by jets of alternating direction. The interior transport is also structured in alternating south-north currents, but of lower amplitude (Figure 7b).

The zonal cumulative sum of transport per water mass for SW, SACW, AAIW and UCDW layers displays a similar pattern. The largest transports are attributed to SACW and AAIW. The transport fluctuations of

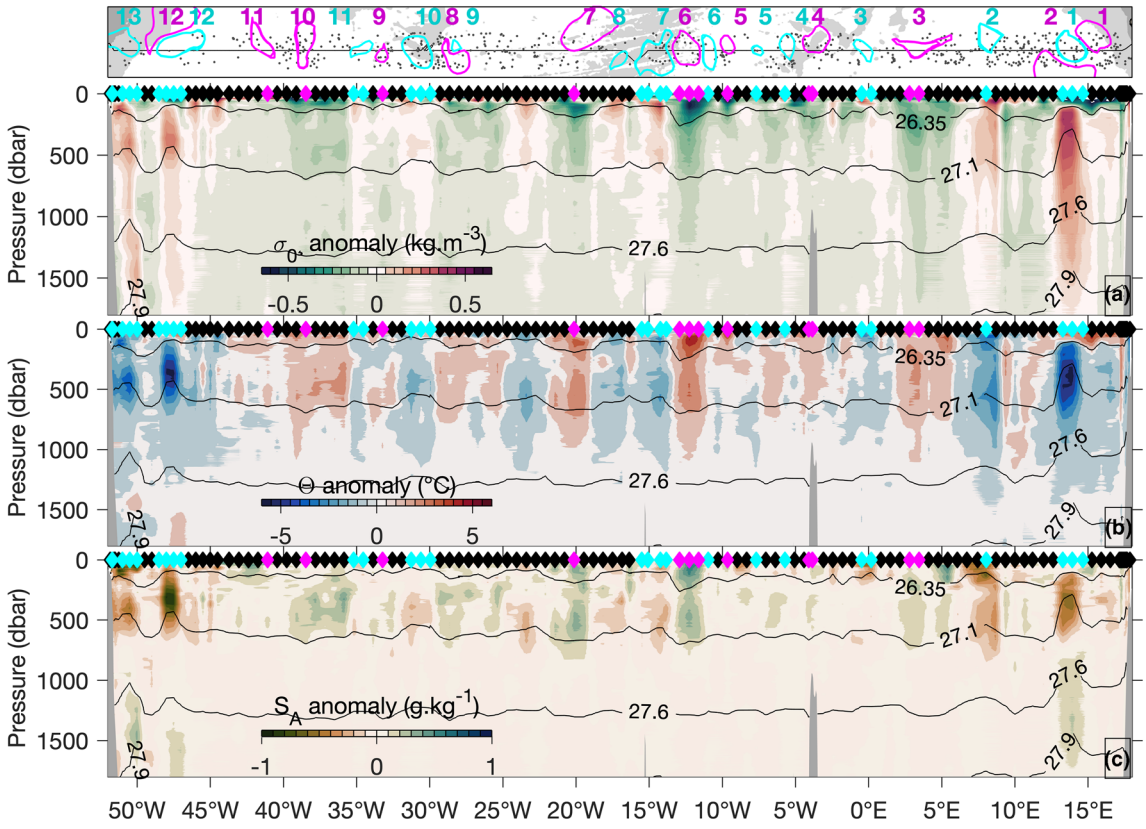

Figure 8. (a) Potential density (σ_0, kg m^{-3}), (b) Conservative temperature (Θ,°C), and (c) Absolute salinity (S_A, g kg^{-1}) anomalies from MSM60 cruise at 34.5ºS in the South Atlantic relative to a summer climatology constructed from non-eddy Argo profiles using the TOEddies database (Laxenaire et al., 2018). Diamonds in the top axis of each panel represent the MSM60 CTD stations colored in black, magenta or cyan depending if the station is outside or within anticyclonic or cyclonic eddies, respectively. The upper panel in (a) shows a map with the cruise track in black, the contours of the anticyclonic and cyclonic eddies with their corresponding number in magenta and cyan respectively, and the gray dots indicate the location of Argo profiles used for producing the climatology. CTD, conductivity-temperature-depth; TOEddies, the ocean eddy detection and tracking algorithm.

these water masses are associated with boundary currents and mesoscale activity. Below, deep and bottom water masses display a more uniform behavior, very likely because they are less influenced by intense mesoscale dynamics. NADW has a negative transport almost across the entire section (from the western continental slope to 3°E) with the strongest transport concentrated at the western boundary. LCDW flows in the opposite direction. Its northward transport is observed across the section, from the western margin to 3°E, although in the middle of the Atlantic, between 30°W and 3°E, LCDW transport is near 0. Between 3°E and 6°E LCDW and NADW transports are directed northward and southward, respectively. From 6°E to 12°E they switch direction. This is probably due to a deep and bottom water recirculation described by various authors in previous studies (Arhan et al., 1999; Gladyshev et al., 2008; Kersalé et al., 2019; Reid, 1989). East of 12°E, transport in both water masses is southward. Finally, recently ventilated AABW transport is mostly northward and is confined between 48°W and 33°W (Figure 7b).

4.4. Vertical Structure of Mesoscale Eddies and Western Boundary Currents

The summer climatology created from non-eddy Argo float profiles in the upper 1,700 dbar allowed to estimate both the contribution of mesoscale eddies to oceanic transport of properties and the anomalies associated with these structures in the water column. Anomalies up to 0.65 kg m^{-3}, 5.5°C, and 0.95 g kg^{-1} in density, conservative temperature and absolute salinity, respectively, are observed in the upper 1,000 dbars associated with mesoscale eddies, with cold and fresh anomalies observed for CEs and warm and salty anomalies for AEs as expected (Figure 8 and S9).

During MSM60, at least four stations were occupied close to the center of mesoscale eddies, two cyclonic (C1 and C12) and two anticyclonic (A3 and A6). C1, the most intense mesoscale structure crossed through its center, displays anomalies that are about twice as large as in the other profiles and extends as deep as 1,600 dbar. Most of the eddies show more intense anomalies between about 100 and 700 dbar, suggesting that they are subsurface intensified. Their identification based on surface properties only (weak ADT, SST) can lead to an underestimation of the anomalies. For example, though C12 presents a positive SST anomaly (3.89°C), while the vertical structure shows intense negative conservative temperature, absolute salinity and positive density anomalies between 100 and 1,200 m depth, clearly indicating that this is a cyclonic cold core eddy. Similarly, A3 and A6 do not show significant SST or salinity anomalies, though their core is warmer and saltier than the surrounding waters (Figure 8).

One clear asymmetry between AEs and CEs is that the absolute maxima in density anomalies are observed immediately above $\gamma^n = 26.35$ kg m^{-3} for AEs (surface intensified negative density anomalies) and immediately below $\gamma^n = 26.35$ kg m^{-3} for cyclonic eddies (subsurface intensified positive density anomalies). The maximum (absolute value) in conservative temperature and absolute salinity anomalies follow the same pattern. Below the thermocline, where stratification is weaker, the vertical displacement of the isopycnals in A3 and A6 is larger than in the upper layers. The intense and deep-reaching eddies like C1 show an inversion in salinity anomalies below 800 dbar essentially impacted by AAIW (Figure 8c).

The vertical structure of three mesoscale eddies (A3, A6, and C12) crossed very close to the center and sampled with at least three CTD profiles exhibit very different characteristics. The easternmost eddy C1 was crossed near the eastern boundary, Anticyclone A6 was crossed east of the Mid-Atlantic Ridge and the westernmost eddy C10 was located west of the Mid-Atlantic Ridge. Differences in sea-level height between the center of the eddy and the maximum velocity contour are 5, 15, and 25 cm for C10, A6 and C1 respectively (Figures 9a–9c). The SADCP and geostrophic (Method 2) meridional velocities are in good agreement (Figures 9d–9i). Every contour of 5 cm in the ADT gradient for a typical radius of 40 km provides 0.15 m s^{-1} surface geostrophic velocities at this latitude, which is also the color interval in Figure 9d–i. The most intense eddy, C1, shows currents of 0.8 m s^{-1} with a stronger northward flow. These three eddies seem to be subsurface intensified and separated from the surface. This is particularly true for C1 whose maximum velocity core lies at 100 dbar. As the ADT gradient decreases, subsurface density anomalies decrease, currents within the eddy tend to get shallower, weaker, and the core region with velocities close to 0 wider (Figure 9d–l).

In the western boundary, the BC appears as a narrow jet (50 km) between 50°W and 49.55°W associated with a large tilt in the isopycnals. The continuous SADCP measurements allowed us to sample the core of the BC at 49.85°W with southward mean velocities of about 0.8 m s^{-1} in the upper 500 dbars. This is nearly 150 km offshore than the usual location of the BC at 51.5°W according to Valla et al., (2018). The BC was surrounded by two cyclonic eddies, C12 and C13. C12 was centered north of 34.5°S and registered the maximum zonal velocity of the section (0.8 m s^{-1}). TOEddies tracked C12 from the Zapiola gyre, with a mean translation speed of about 8 km per day, nearly double that of the other CEs crossed (Figure 2b). SADCP, ship-mounted acoustic doppler current profilers.

The volume transport between 50°W and 49.55°W associated with western boundary currents (BC and Deep Western Boundary Current) was particularly intense, with a maximum transport of −35.60 Sv between surface and 2,827 dbar from from ADCPs (Method 1), and −46.19 Sv from surface to 2,842 dbar from geostrophy (Method 2), respectively. Identifying the limit between the BC and the Deep Western Boundary Current can be difficult as both currents flow southward near the slope. In the upper 1,000 dbars, both methods display a strong jet with a mean meridional velocity about −0.5 m s^{-1}. Below 1,000 dbar, the southward jet displays a progressively offshore shift in the downward direction, as observed by Valla et al. (2018; Figure 10).

The BC volume transport from surface to 500 dbar, a common reported value, during MSM60 is −13.97–−15.87 Sv from Method 1 and 2, respectively. In the upper 800 dbars, both methods display a volume transport of −20.86−−23.46, respectively. Our estimates agree to the −19.4 Sv at 35°S reported by S. L. Garzoli et al., (2013) from 17 XBTs transects in the upper 800 m, and also with Schmid & Majumder (2018; and references therein) who estimate a volume transport of -17.3 ± 3.5 Sv combining Argo floats and sea surface

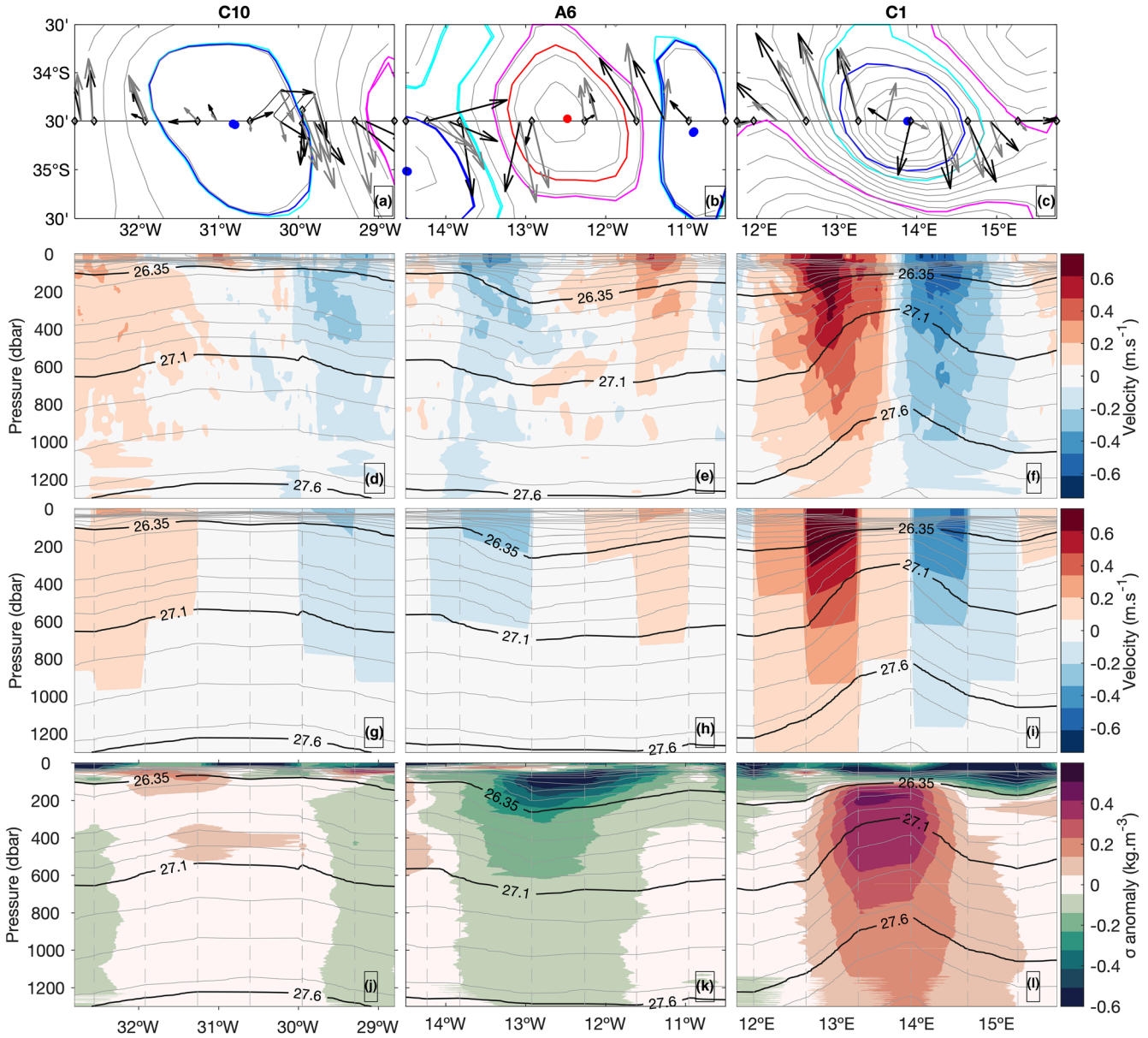

Figure 9. Three mesoscale eddies crossed through their center during MSM60. Each column corresponds to a specific eddy and each row to one property. (a–c) Absolute Dynamic Topography (ADT) observed from satellite altimetry (gray contours, 5 cm contour interval). The black line shows the cruise track over 34.5°S and the black diamonds the CTD profiles location. Black and gray arrows represent the ocean current velocity vectors calculated from altimetry and geostrophy (averaged over the upper 100 m), respectively. Cyan (magenta) and blue (red) contours represent the outermost and maximum velocity contours of the cyclonic (anticyclonic) eddies, respectively. The dot represents the eddy centroid. (d–f) SADCP velocity. Black contours show neutral density isolines. (g–i) Geostrophic velocity calculated relative to $\gamma = 28.1$ kg m^{-3} and then mass balanced. Black contours show neutral density isolines. The dashed line shows the CTD profile positions. (j–l) Vertical profiles of potential density anomaly (kg m^{-3}) calculated relative to the summer non-eddy Argo climatology.

height, also in the upper 800 m. The reason for our higher (~4 Sv) values could be related not only to the temporal variability of the BC but also with the high-resolution data used here, allowing to sample the sharp gradients associated with the boundary current.

4.5. Comparison with Nearby GO-SHIP Transects

Given the sensitivity of the transport estimates to the method used, a final analysis was undertaken to compare our results with nearby GO-SHIP sections A09 at 24°S (King & Hamersley, 2010), A10 at 30ºS (M.

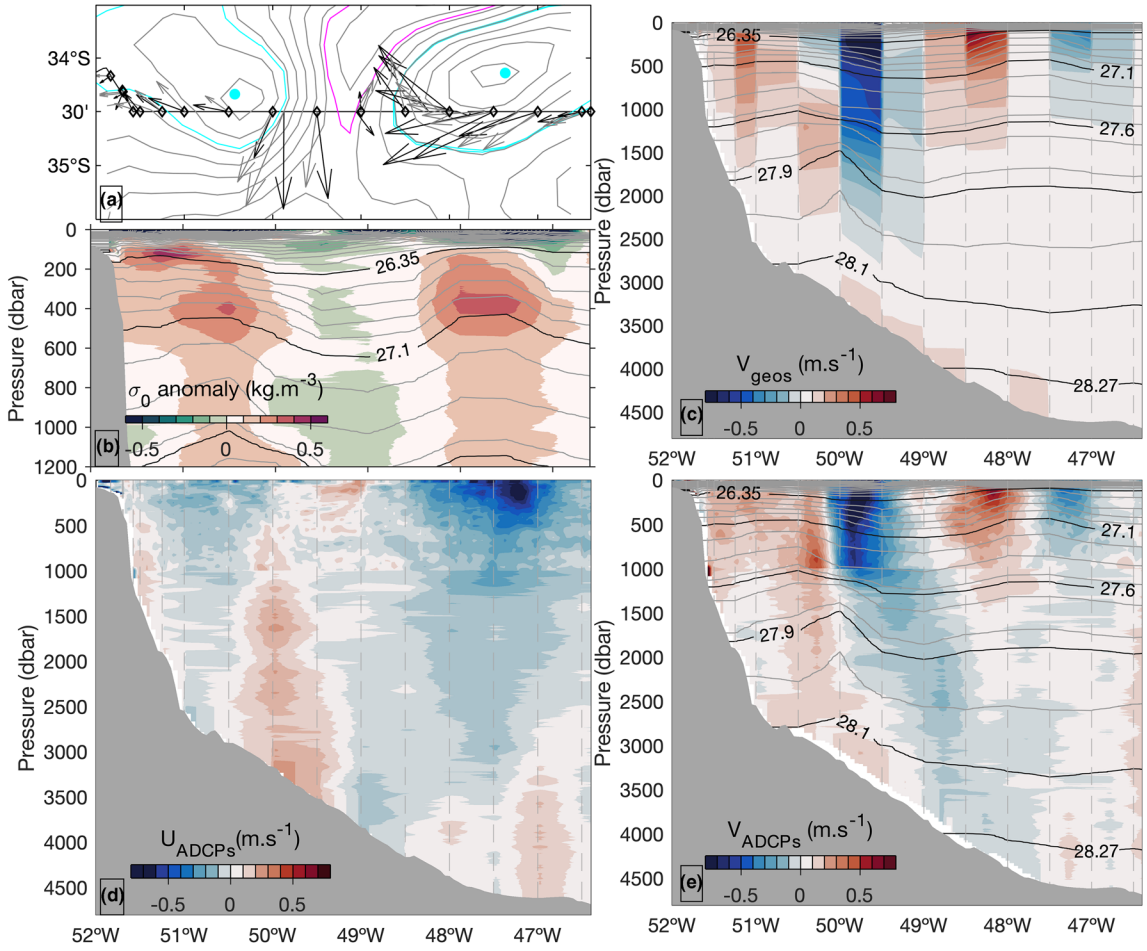

Figure 10. South Atlantic western boundary velocity structure at 34.5°S during the MSM60 cruise. (a) Horizontal map of the satellite derived absolute dynamic topography with isolines every 5 cm in gray. The black line shows the cruise track over 34.5°S. Black and gray arrows represent the ocean current velocity vectors calculated from altimetry and geostrophy (averaged over the upper 100 m), respectively. Cyan and magenta contours represent the maximum velocity contours of the cyclonic and anticyclonic eddies, respectively. (b) Vertical profile of potential density anomaly (kg m^{-3}) relative to a non-eddy Argo climatology for summer. (c) Geostrophic velocity (method 1). Black contours show neutral density isolines. (d) Zonal and (e) Meridional Velocity from ADCPs. The abrupt change in the horizontal resolution at 1000 dbar is due to the change from the SADCP observations gridded every 0.05° to the LADCP observations restricted to the CTD profiles approximately every 0.5°. CTD, conductivity-temperature-depth; LADCP, lowered acoustic doppler current profilers; SADCP, ship-mounted acoustic doppler current profilers.

Baringer & Macdonald, 2013) and MSM60 at 34.5°S (Table 4). Following the same approach as Method 2, all data were gridded into a 0.05° by 1 dbar across the main latitude of each section. Then, we computed the geostrophic velocity relative to γ^n = 28.1 kg m^{-3} as level of no motion, added the Ekman transport in the upper 50 dbar and then added a uniform barotropic velocity in order to achieve mass balance. It is important to underline that the zonal distance between grid point is different due to latitudinal variations, with 0.05° representing 5058, 4812 and 4,579 m for 24°S, 30°S and 34.5°S, respectively.

Table 4
Volume Transport, Meridional Heat Transport (MHT) and Freshwater Transport (MFT) Estimates of the Meridional Overturning Circulation Through the Different trans-Atlantic Sections in This Study Applying the Same Methodology: γ^n = 28.1 kg m^{-3} as Level of No Motion and Equally Distributing the Imbalance Assumed as the Barotropic Flow

Section	Date	AMOC (Sv-dbar)	MHT (PW)	MFT (Sv)
A09 24°S	Mar/09	24.47–1275	1.08	−0.23
A10 30°S	Oct/11	20.43–1208	0.65	−0.02
MSM60 34.5°S	Jan/17	15.18–1175	0.23	0.21

Overall, the results are consistent with previous studies (e.g., Ganachaud & Wunsch, 2003). The computed AMOC volume transports are 24.47, 20.43 and 15.18 Sv, and MHT values are 1.08, 0.65 and 0.23 PW at 24°S, 30°S and 34.5°S, respectively (Table 4). Both, the northward heat transport across all three sections and the AMOC strength increase northward from 34.5°S. The increase rate is nearly linear between 34.5°S and 24°S, being 0.09 PW and 0.08 PW, 1.17 Sv and 1.50 Sv per degree latitude from

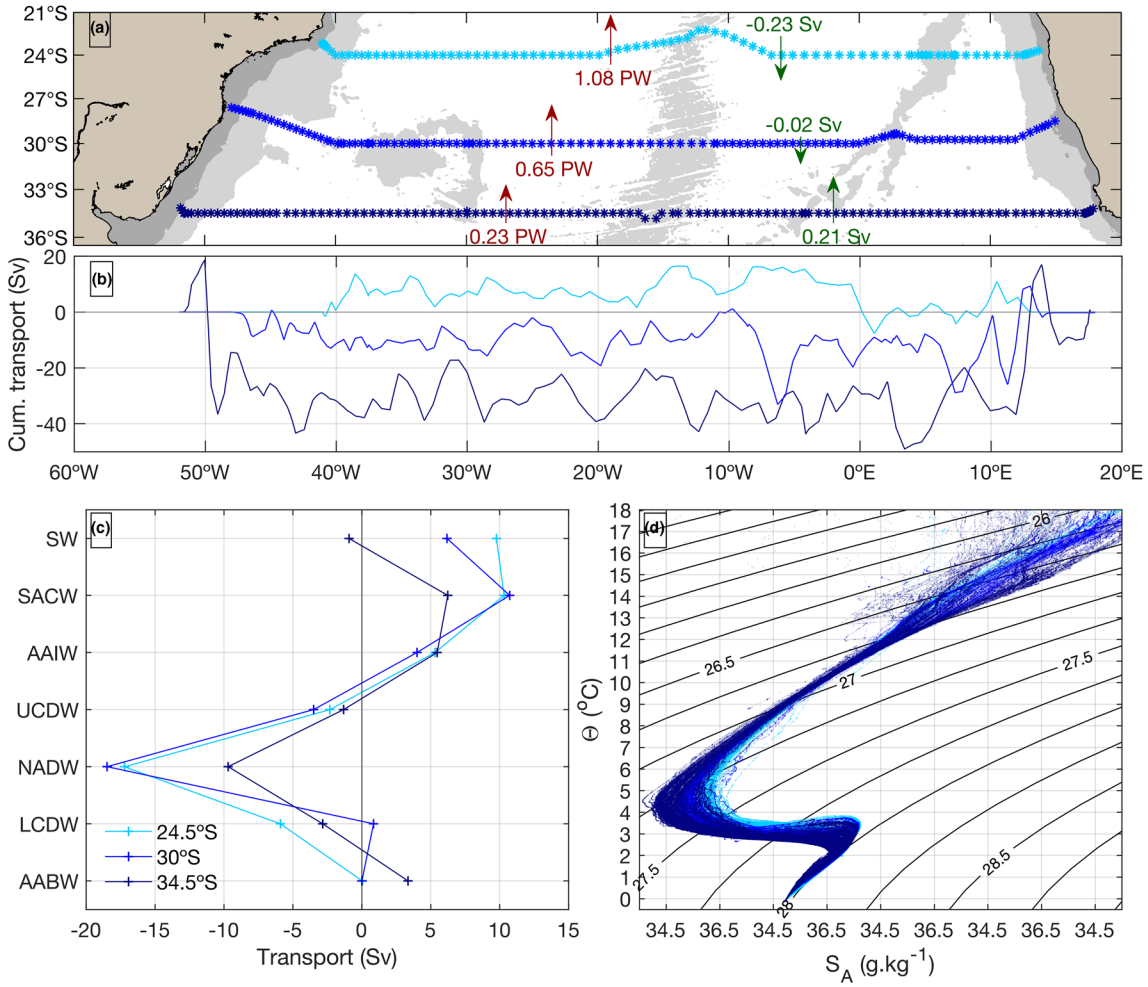

Figure 11. Transport and water masses comparison in the South Atlantic from 3 GO-SHIP sections (A9, A10, and MSM60; see Table 3 for details). (a) CTD positions for A9 (light blue), A10 (blue), and MSM60 (dark blue). The arrows show the net heat (red) and freshwater (green) transports per section. The gray shading represents water depths less than 200 and 3,500 m in the ETOPO2 data set (Smith & Sandwell, 1997). Colors for each section are the same in all panels. (b) Cumulative vertically integrated meridional transport from west to east for the three sections. (c) Transport by water mass layer (see Table 2 for references) (d) Θ-S_A diagram.

34.5 ºS to 30ºS and from 30°S to 24°S, respectively. The latitudinal MHT changes in the upper limb of the SAMOC at 34.5°S relative to the A10 and A09 fluxes are mainly due to the northward transport increase in the upper layers (SW to SACW). SW transport is particularly intense and northward at 24°S (9.9 Sv), less intense at 30°S (6.1 Sv), and negative at 34.5°S (−0.4 Sv). SACW transport is close to 10 Sv at 24°S and 30°S and 7.35 Sv at 34.5°S. NADW is also about 6 Sv larger at lower latitudes than at 34.5°S (Figures 11c and Table 4).

The lower value of MHT at 34.5°S compared to the other two northern sections is partially explained by the intense southward transport of the BC during MSM60 (Peterson & Stramma, 1991; Figure 11b). Moreover, mesoscale eddies also play a role in the upper limb transport. At 34.5°S, mesoscale activity is more energetic than at 30°S and 24°S (Laxenaire et al., 2018). Freshwater transport estimates show a convergence toward the center of the South Atlantic gyre, as expected from the method used (Buckley & Marshall, 2016), with negative values of −0.23 Sv and −0.02 Sv at 24°S and 30°S, while at 34.5°S freshwater transport is 0.21 Sv (Table 4, Figure 11a). The implied freshwater convergence obtained between these latitudes (24°–34.5°S) is quite large as the evaporation needed to achieve that balance should be about three times larger than the annual mean (A. L. Gordon & Piola, 1983). The high sensitivity of the method, and the salt export through the Bering Strait (27.6 10^6 kg s^{-1}, Coachman & Aagaard, 1988), not considered here could explain the large value obtained.

The abyssal overturning cell appears clearly only at 34.5°S, although it is known that AABW flows northward through the Vema Channel at 30°S. However, as only one CTD station was carried out in the Vema Channel during A10 it was not possible to estimate the geostrophic transport there. NADW transport decreases from near −18 Sv at 24°S to −10.84 Sv 34.5°S. At 24°S there is no AABW nor abyssal overturning cell. The northward limit of the abyssal cell seems to be close to 30°S, confining the AABW flow to the deep Vema and Hunter Channels as suggested also by previous studies (e.g., Hogg et al., 1982; Valla et al., 2019). Finally, although all the sections compared were done in austral spring or summer, observations and models show that the annual cycle in meridional heat transport can account for more than 30% of the variance and should also be considered for comparisons (e.g., Dong et al., 2014). This also emphasizes the need for more regular observations which are able to capture and account for the variations in the annual cycle.

5. Conclusions

This study provides a first description of the water mass structure, currents and meridional volume, heat, and freshwater transport along 34.5°S in the South Atlantic Ocean. The meridional circulation of the upper, deep and abyssal layers is described from direct observations for the first time and complements the efforts by the SAMOC international initiative to determine and monitor the meridional circulation at this latitude, which is a hot spot for the entire AMOC. We also describe and discuss the mesoscale eddy structures encountered during the cruise. Such mesoscale features explain most of the transbasin variability observed in the upper 1,000 dbar.

At 34.5°S we find the abyssal overturning cell is weaker (2.4 $\pm$ 1.6 Sv) than the upper cell (15.64 $\pm$ 1.39 Sv) and it consists of northward flow of AABW confined to the western basin. Across the section, a net meridional heat transport of 0.27 $\pm$ 0.10 PW is observed from geostrophic approximations and 0.26 PW from direct velocity observations (corrected for the mass imbalance over the section). These heat transport estimates are lower than previously reported (~0.5 PW, Dong et al., 2015) and could be explained by the relatively low intensity of the upper overturning cell during the cruise compared with the mean reported from moorings (Kersalé et al., 2020) and the anomalous predominance of cold core eddies. In comparisons with neighboring transbasin sections, applying the same analysis methods, we find that the AMOC volume transport and MHT increased toward the equator (0.65 PW at 30°S and 1.08 PW at 24°S). This agrees with previous results indicating this unique characteristic of the equatorial MHT in the South Atlantic, and can be explained by the intensified northward transport and warm waters in the upper layers being compensated by southward flow of relatively cold NADW at depth. The decrease in strength of the upper overturning cell is, among other phenomena, associated with the intensification of the warm Brazil Current (BC) flowing southward between 24°S and 34.5°S, and to a minor extent mesoscale activity, leading to a weakening of the AMOC with increasing latitude (from 24.47 Sv at 24°S to 15.18 Sv at 34.5°S).

One unique value of transbasin sections is having access to hydrographic properties and the flow field at the same time. From the 34.5°S section we identify the existence of more recently ventilated water masses on the western side of the basin and older waters in the east. The major differences in oxygen and thermohaline composition were observed within the AAIW, NADW, and LCDW layers. AAIW is directly injected from the Brazil-Malvinas Confluence region in the west while in the east is supplied mostly from the Indian Ocean and therefore is saltier, warmer and less oxygenated. NADW flows southward and reaches 34.5°S along both boundaries. Because of the indirect path, the eastern NADW branch is less salty and less oxygenated. LCDW is warmer and saltier in the eastern part of the section and also the transport changes sign across the basin, flowing northward in the western part and southward in the eastern part.

Highest velocities are observed in the BC while transient, mesoscale eddies with high but alternating velocities are evident in the upper 500 m of the section. The eddies also carry water mass anomalies that originate from the Indian Ocean and subantarctic waters originated from the Pacific before they dissolve near the Brazil-Malvinas confluence. We find that the eddies have only a small impact on the upper overturning cell but the MHT almost doubled when the eddies (predominantly cold core eddies) were removed. It should also be noted that during the cruise we observed an anomalous predominance of CEs over AEs.

Whereas our results confirm previous findings that the South Atlantic circulation sets preferential paths for inter-oceanic exchanges and actively participates in the transformation of water masses, particularly in

regions of high mesoscale activity (e.g., S. L. Garzoli & Matano, 2011; Speich et al., 2007), they also show the need of high-resolution observations, especially near the boundaries, to correctly resolve the meridional transports.

Data Availability Statement

The data from the MSM60 cruise are available at: https://doi.org/10.2312/cr_msm60. ADT data were downloaded from http://marine.copernicus.eu/, SST from https://podaac.jpl.nasa.gov/, eddy tracking from https://vesg.ipsl.upmc.fr/thredds/catalog/IPSLFS/rlaxe/catalog.html?data set=DatasetScanIPSLFS/rlaxe/Database_ South_Atl.zip. GO-SHIP datasets were downloaded from http://cchdo.ucsd.edu.

Acknowledgments
The authors declare to have no conflict of interest and deeply acknowledge all the people on board MSM60, the SAMOC-SAMBAR team, and all the open access datasets. This work was supported by the European Union's Horizon 2020 research and innovation program under grant agreements no. 633211 (AtlantOS) and no. 817578 (TRIATLAS), the TOEddies CNES-TOSCA research grant. In addition, this work was further supported under the South African NRF grants UID 110733 and 118901. G. Manta received funding from bourse ANII-Campus France (POS_CFRA_2017_1_146868). M. Kersalé was supported in part under the auspices of the Cooperative Institute for Marine and Atmospheric Studies (CIMAS), a Cooperative Institute of the University of Miami and the National Oceanic and Atmospheric Administration (NOAA), cooperative agreement NA20OAR4320472. M. Kersalé and C. S. Meinen also acknowledge additional support from the NOAA Atlantic Oceanographic and Meteorological Laboratory. R. Hummels acknowledges support from the German Federal Ministry of Education and Research as part of the cooperative project RACE (03F0605 B, 03F0824 C) and the European Union's Horizon 2020 research and innovation program under grant agreement 817578 TRIATLAS project. SAMBAR Project is funded by the Sao Paulo State Research Foundation (FAPESP, grants 2011/50552-4 and 2017/09659-6). T. Lamont, M.A. van den Berg, and I. Ansorge received funding from the South African National Research Foundation (no. 110733) as well as the Department of Environment, Forestry and Fisheries. The authors also acknowledge the mesoscale calculation server CICLAD (http://ciclad-web.ipsl.jussieu.fr) dedicated to Institut Pierre Simon Laplace modeling and data analyses effort for technical and computational support.

References

Almeida, L., de Azevedo, J. L. L., Kerr, R., Araujo, M., & Mata, M. M. (2018). Impact of the new equation of state of seawater (TEOS-10) on the estimates of water mass mixture and meridional transport in the Atlantic Ocean. *Progress in Oceanography*, *162*, 13–24. https://doi.org/10.1016/j.pocean.2018.02.008

Ansorge, I. J., Baringer, M. O., Campos, E. J., Dong, S., Fine, R. A., Garzoli, S. L., & Roberts, M. J. (2014). Basin-wide oceanographic array bridges the South Atlantic. *Eos, Transactions American Geophysical Union*, *95*(6), 53–54. https://doi.org/10.1002/2014EO060001

Argo. (2020). Argo float data and metadata from Global Data Assembly Centre (Argo GDAC). *SEANOE*. https://doi.org/10.17882/42182

Arhan, M., Mercier, H., & Lutjeharms, J. R. E. (1999). The disparate evolution of three Agulhas rings in the South Atlantic Ocean. *Journal of Geophysical Research*, *104*(C9), 20987–21005. https://doi.org/10.1029/1998JC900047

Arhan, M., Mercier, H., & Park, Y. H. (2003). On the deep water circulation of the eastern South Atlantic Ocean. *Deep Sea Research Part I: Oceanographic Research Papers*, *50*(7), 889–916. https://doi.org/10.1016/S0967-0637(03)00072-4

Artana, C., Provost, C., Lellouche, J.-M., Rio, M.-H., Ferrari, R., & Sennéchael, N. (2019). The Malvinas Current at the confluence with the Brazil Current: Inferences from 25 years of Mercator ocean reanalysis. *Journal of Geophysical Research: Oceans*, *124*, 7178–7200. https://doi.org/10.1029/2019JC015289

Baringer, M. O., & Garzoli, S. L. (2007). Meridional heat transport determined with expendable bathythermographs—Part I: Error estimates from model and hydrographic data. *Deep Sea Research Part I: Oceanographic Research Papers*, *54*(8), 1390–1401. https://doi.org/10.1016/j.dsr.2007.03.011

Baringer, M., & Macdonald, A. (2013). *A10 Cruise Summary Information*. Downloaded from. https://cchdo.ucsd.edu/cruise/33RO20110926

Belkin, I. M., & Gordon, A. L. (1996). Southern Ocean fronts from the Greenwich meridian to Tasmania. *Journal of Geophysical Research: Oceans*, *101*(C2), 3675–3696. https://doi.org/10.1029/95JC02750

Bentamy, A., & Fillon, D. C. (2012). Gridded surface wind fields from Metop/ASCAT measurements. *International Journal of Remote Sensing*, *33*(6), 1729–1754. https://doi.org/10.1080/01431161.2011.600348

Biastoch, A., Böning, C. W., & Lutjeharms, J. R. E. (2008). Agulhas leakage dynamics affects decadal variability in Atlantic overturning circulation. *Nature*, *456*(7221), 489–492. https://doi.org/10.1038/nature07426

Boebel, O., Davis, R. E., Ollitrault, M., Peterson, R. G., Richardson, P. L., Schmid, C., & Zenk, W. (1999). The intermediate depth circulation of the western South Atlantic. *Geophysical Research Letters*, *26*(21), 3329–3332. https://doi.org/10.1029/1999GL002355

Bryden, H. L., & Imawaki, S. (2001). *Ocean heat transport. In: International Geophysics* (77 pp. 455–474). Academic Press. https://doi.org/10.1016/S0074-6142(01)80134-0

Bryden, H. L., King, B. A., & McCarthy, G. D. (2011). South Atlantic overturning circulation at 24ºS. *Journal of Marine Research*, *69*(1), 38–55. https://doi.org/10.3389/fmars.2019.00260

Buckley, M. W., & Marshall, J. (2016). Observations, inferences, and mechanisms of the Atlantic Meridional Overturning Circulation: A review. *Reviews of Geophysics*, *54*, 5–63. https://doi.org/10.1002/2015RG000493

Callahan, J. E. (1972). The structure and circulation of deep water in the Antarctic. Deep sea research and oceanographic abstracts (Vol. *19*, No. 8, pp. 563–575). Elsevier.

Capet, A., Mason, E., Rossi, V., Troupin, C., Faugère, Y., Pujol, I., & Pascual, A. (2014). Implications of refined altimetry on estimates of mesoscale activity and eddy-driven offshore transport in the eastern boundary upwelling systems. *Geophysical Research Letters*, *41*(21), 7602–7610. https://doi.org/10.1002/2014GL061770

Capuano, T. A., Speich, S., Carton, X., & Laxenaire, R. (2018). Indo-Atlantic exchange, Mesoscale dynamics, and Antarctic intermediate water. *Journal of Geophysical Research: Oceans*, *123*(5), 3286–3306. https://doi.org/10.1002/2017JC013521

Chidichimo, M. P., Kanzow, T., Cunningham, S. A., & Marotzke, J. (2010). The contribution of eastern boundary density variations to the North Atlantic meridional overturning circulation at 26, 5°N. *Ocean Science*, *6*, 475–490. https://doi.org/10.5194/os-6-475-2010

Chin, T. M., Vazquez-Cuervo, J., & Armstrong, E. M. (2017). A multi-scale high-resolution analysis of global sea surface temperature. *Remote Sensing of Environment*, *200*, 154–169. https://doi.org/10.1016/j.rse.2017.07.029

Cimatoribus, A. A., Drijfhout, S. S., Den Toom, M., & Dijkstra, H. A. (2012). Sensitivity of the Atlantic meridional overturning circulation to South Atlantic freshwater anomalies. *Climate Dynamics*, *39*(9–10), 2291–2306. https://doi.org/10.1007/s00382-012-1292-5

Coachman, L. K., & Aagaard, K. (1988). Transports through Bering Strait: Annual and interannual variability. *Journal of Geophysical Research: Oceans*, *93*(C12), 15535–15539. https://doi.org/10.1029/JC093iC12p15535

Cunningham, S. A., Kanzow, T., Rayner, D., Baringer, M. O., Johns, W. E., Marotzke, J., & Meinen, C. S. (2007). Temporal variability of the Atlantic meridional overturning circulation at 26.5°N. *Science*, *317*(5840), 935–938. https://doi.org/10.1126/science.1141304

Dong, S., Baringer, M. O., Goni, G. J., Meinen, C. S., & Garzoli, S. L. (2014). Seasonal variations in the South Atlantic meridional overturning circulation from observations and numerical models. *Geophysical Research Letters*, *41*, 4611–4618. https://doi.org/10.1002/2014GL060428

Dong, S., Garzoli, S., Baringer, M., Meinen, C., & Goni, G. (2009). Interannual variations in the Atlantic meridional overturning circulation and its relationship with the net northward heat transport in the South Atlantic. *Geophysical Research Letters*, *36*(20), L20606. https://doi.org/10.1029/2009GL039356

Dong, S., Goni, G., & Bringas, F. (2015). Temporal variability of the South Atlantic meridional overturning circulation between 20°S and 35°S. *Geophysical Research Letters*, *42*(18), 7655–7662. https://doi.org/10.1002/2015GL065603

Drijfhout, S. S., Weber, S. L., & van der Swaluw, E. (2011). The stability of the MOC as diagnosed from model projections for pre-industrial, present and future climates. *Climate Dynamics*, *37*(7–8), 1575–1586. https://doi.org/10.1007/s00382-010-0930-z

Duacs/AVISO+ (2015). SSALTO/DUACS user handbook:(M) SLA and (M) ADT near-real time and delayed time products (vol. 6, pp. 74). CLS-DOS-NT-06-034.

Frajka-Williams, E., Cunningham, S. A., Bryden, H., & King, B. A. (2011). Variability of Antarctic Bottom Water at 24.5°N in the Atlantic. *Journal of Geophysical Research*, *116*, C11026. https://doi.org/10.1029/2011jc007168

Frajka-Williams, E., Ansorge, I. J., Baehr, J., Bryden, H. L., Chidichimo, M. P., Cunningham, S. A., & Holliday, N. P. (2019). Atlantic meridional overturning circulation: Observed transports and variability. *Frontiers in Marine Science*, *6*, 260. https://doi.org/10.3389/fmars.2019.00260

Ganachaud, A., & Wunsch, C. (2003). Large-scale ocean heat and freshwater transports during the World Ocean Circulation Experiment. *Journal of Climate*, *16*(4), 696–705. https://doi.org/10.1175/1520-0442(2003)016<0696:LSOHAF>2.0.CO;2

Garzoli, S. L., & Baringer, M. O. (2007). Meridional heat transport determined with expandable bathythermographs—Part II: South Atlantic transport. *Deep Sea Research Part I: Oceanographic Research Papers*, *54*(8), 1402–1420. https://doi.org/10.1016/j.dsr.2007.04.013

Garzoli, S. L., Baringer, M. O., Dong, S., Perez, R. C., & Yao, Q. (2013). South Atlantic meridional fluxes. *Deep-Sea Research Part I*, *71*, 21–32. https://doi.org/10.1016/j.dsr.2012.09

Garzoli, S. L., & Matano, R. (2011). The South Atlantic and the Atlantic meridional overturning circulation. *Deep Sea Research Part II: Topical Studies in Oceanography*, *58*(17–18), 1837–1847. https://doi.org/10.1016/j.dsr2.2010.10.063

Georgi, D. T. (1981). On the relationship between the large-scale property variations and fine structure in the circumpolar deep water. *Journal of Geophysical Research*, *86*(C7), 6556–6566. https://doi.org/10.1029/JC086iC07p06556

Gladyshev, S., Arhan, M., Sokov, A., & Speich, S. (2008). A hydrographic section from South Africa to the southern limit of the Antarctic circumpolar current at the Greenwich meridian. *Deep Sea Research Part I: Oceanographic Research Papers*, *55*(10), 1284–1303. https://doi.org/10.1016/j.dsr.2008.05.009

Gordon, A. L. (1981). South Atlantic thermocline ventilation. *Deep Sea Research Part I*, *28*, 1239–1264. https://doi.org/10.1016/0198-0149(81)90033-9

Gordon, A. L. (1985). Indian-Atlantic transfer of thermocline water at the Agulhas retroflection. *Science*, *227*(4690), 1030–1033. https://doi.org/10.1126/science.227.4690.1030

Gordon, A. L. (1986). Interocean exchange of thermocline water. *Journal of Geophysical Research*, *91*(C4), 5037–5046. https://doi.org/10.1029/JC091iC04p05037

Gordon, A. L., Lutjeharms, J. R., & Gründlingh, M. L. (1987). Stratification and circulation at the Agulhas retroflection. *Deep Sea Research Part A: Oceanographic Research Papers*, *34*(4), 565–599. https://doi.org/10.1016/0198-0149(87)90006-9

Gordon, A. L., & Piola, A. R. (1983). Atlantic Ocean upper layer salinity budget. *Journal of Physical Oceanography*, *13*(7), 1293–1300. https://doi.org/10.1175/1520-0485(1983)013<1293:AOULSB>2.0.CO;2

Gordon, A. L., Weiss, R. F., Smethie, W. M., Jr, & Warner, M. J. (1992). Thermocline and intermediate water communication between the South Atlantic and Indian Oceans. *Journal of Geophysical Research*, *97*(C5), 7223–7240. https://doi.org/10.1029/92JC00485

Guerra, L. A. A., Paiva, A. M., & Chassignet, E. P. (2018). On the translation of Agulhas rings to the western South Atlantic Ocean. *Deep Sea Research Part I: Oceanographic Research Papers*, *139*, 104–113. https://doi.org/10.1016/j.dsr.2018.08.005

Hernández-Guerra, A., & Talley, L. D. (2016). Meridional overturning transports at 30°S in the Indian and Pacific Oceans in 2002–2003 and 2009. *Progress in Oceanography*, *146*, 89–120. https://doi.org/10.1016/j.pocean.2016.06.005

Hernández-Guerra, A., Talley, L. D., Pelegrí, J. L., Vélez-Belchí, P., Baringer, M. O., Macdonald, A. M., & McDonagh, E. L. (2019). The upper, deep, abyssal and overturning circulation in the Atlantic Ocean at 30°S in 2003 and 2011. *Progress in Oceanography*, *176*, 102136. https://doi.org/10.1016/j.pocean.2019.102136

Herrford, J., Brandt, P., Kanzow, T., Hummels, R., Araujo, M., & Durgadoo, J. V. (2020). Seasonal variability of the Atlantic meridional overturning circulation at 11°S inferred from bottom pressure measurements. *Ocean Science Discussions*, *In review*, 1–37. https://doi.org/10.5194/os-2020-55

Hogg, N., Biscaye, P., Gardner, W., & Schmitz, W. J., Jr (1982). On the transport and modification of Antarctic Bottom Water in the Vema Channel. *Journal of Marine Research*, *40*(23), l–263.

Holfort, J., & Siedler, G. (2001). The meridional oceanic transports of heat and nutrients in the South Atlantic. *Journal of Physical Oceanography*, *31*(1), 5–29. https://doi.org/10.1175/1520-0485(2001)031<0005:TMOTOH>2.0.CO;2

Holliday, N. P., Bacon, S., Cunningham, S. A., Gary, S. F., Karstensen, J., King, B. A., & Mcdonagh, E. L. (2018). Subpolar North Atlantic overturning and gyre-scale circulation in the summers of 2014 and 2016. *Journal of Geophysical Research: Oceans*, *123*(7), 4538–4559. https://doi.org/10.1029/2018JC013841

E. M. Hood, C. L. Sabine, & B. M. Sloyan (Eds.), (2010).*The GO-SHIP repeat hydrography manual: A collection of expert reports and guidelines. IOCCP report number 14, ICPO publication series number 134*. Retrieved From http://www.go-ship.org/HydroMan.html

Hsiung, J. (1985). Estimates of global oceanic meridional heat transport. *Journal of Physical Oceanography*, *15*(11), 1405–1413. https://doi.org/10.1175/1520-0485(1985)015<1405:EOGOMH>2.0.CO;2

Johns, W. E., Baringer, M. O., Beal, L. M., Cunningham, S. A., Kanzow, T., Bryden, H. L., & Curry, R. (2011). Continuous, array-based estimates of Atlantic Ocean heat transport at 26.5°N. *Journal of Climate*, *24*(10), 2429–2449. https://doi.org/10.1175/2010JCLI3997.1

Kanzow, T., Cunningham, S. A., Johns, W. E., Hirschi, J. J., Marotzke, J., Baringer, M. O., & Bryden, H. L. (2010). Seasonal variability of the Atlantic meridional overturning circulation at 26.5°N. *Journal of Climate*, *23*(21), 5678–5698. https://doi.org/10.1175/2010JCLI3389.1

Karstensen, J., Speich, S., Asdar, S., Berbel, G. B. B., Branlard, L., Carvalho, A., et al. (2019). *Seamount observatory and SAMOC overturning, cruise No. MSM60, January 04 – February 01, 2017*. Cape Town (South Africa)-Montevideo (Uruguay): MARIA S. MERIAN-Berichte, Gutachterpanel Forschungsschiffe. https://doi.org/10.2312/cr_msm60

Kersalé, M., Lamont, T., Speich, S., Terre, T., Laxenaire, R., Roberts, M. J., & Ansorge, I. J. (2018). Moored observations of mesoscale features in the Cape Basin: characteristics and local impacts on water mass distributions. *Ocean Science*, *14*, 923–945. https://doi.org/10.5194/os-14-923-2018

Kersalé, M., Meinen, C. S., Perez, R. C., Le Hénaff, M., Valla, D., Lamont, T., & Garzoli, S. (2020). Highly variable upper and abyssal overturning cells in the South Atlantic. *Science Advances*, *6*(32), eaba7573. https://doi.org/10.1126/sciadv.aba7573

Kersalé, M., Perez, R. C., Speich, S., Meinen, C. S., Lamont, T., Le Hénaff, M., & Schmid, C. (2019). Shallow and deep eastern boundary currents in the South Atlantic at 34.5 S: Mean structure and variability. *Journal of Geophysical Research: Oceans*, *124*(3), 1634–1659. https://doi.org/10.1029/2018JC014554

B. A. King, & D. R. C. Hamersley (Eds.), (2010). *RSS James Cook cruise JC032, 07 Mar–21 Apr 2009: Hydrographic sections across the Brazil current and at 24°S in the Atlantic* (*48*, pp. 173). National Oceanography Centre Southampton Cruise Report.

Laxenaire, R., Speich, S., Blanke, B., Chaigneau, A., Pegliasco, C., & Stegner, A. (2018). Anticyclonic eddies connecting the western boundaries of Indian and Atlantic oceans. *Journal of Geophysical Research: Oceans*, *123*(11), 7651–7677. https://doi.org/10.1029/2018JC014270

Laxenaire, R., Speich, S., & Stegner, A. (2019). Evolution of the thermohaline structure of one Agulhas ring reconstructed from Satellite altimetry and Argo floats. *Journal of Geophysical Research: Oceans*, *124*, 8969–9003. https://doi.org/10.1029/2018JC014426

Lopez, H., Dong, S., Lee, S. K., & Goni, G. (2016). Decadal modulations of interhemispheric global atmospheric circulations and monsoons by the South Atlantic meridional overturning circulation. *Journal of Climate*, *29*(5), 1831–1851. https://doi.org/10.1175/JCLI-D-15-0491.1

Lozier, M. S., Bacon, S., Bower, A. S., Cunningham, S. A., De Jong, M. F., De Steur, L., & Heimbach, P. (2017). Overturning in the subpolar north Atlantic program: A new international ocean observing system. *Bulletin of the American Meteorological Society*, *98*(4), 737–752. https://doi.org/10.1175/BAMS-D-16-0057.1

Lozier, M. S., Li, F., Bacon, S., Bahr, F., Bower, A. S., Cunningham, S. A., & Gary, S. F. (2019). A Sea change in our view of overturning in the subpolar North Atlantic. *Science*, *363*(6426), 516–521. https://doi.org/10.1126/science.aau6592

Lumpkin, R., & Speer, K. (2007). Global ocean meridional overturning. *Journal of Physical Oceanography*, *37*(10), 2550–2562. https://doi.org/10.1175/JPO3130.1

Lutjeharms, J. R. E., De Ruijter, W. P. M., & Peterson, R. G. (1992). Interbasin exchange and the Agulhas retroflection; the development of some oceanographic concepts. *Deep Sea Research Part A: Oceanographic Research Papers*, *39*(10), 1791–1807. https://doi.org/10.1016/0198-0149(92)90029-S

Lutjeharms, J. R. E., & Gordon, A. L. (1987). Shedding of an Agulhas ring observed at sea. *Nature*, *325*(6100), 138–140.

Majumder, S., Schmid, C., & Halliwell, G. (2016). An observations and model-based analysis of meridional transports in the South Atlantic. *Journal of Geophysical Research: Oceans*, *121*(8), 5622–5638. https://doi.org/10.1002/2016JC011693

McCarthy, G., McDonagh, E., & King, B. (2011). Decadal variability of thermocline and intermediate waters at 24 S in the South Atlantic. *Journal of Physical Oceanography*, *41*(1), 157–165. https://doi.org/10.1175/2010JPO4467.1

McCartney, M. S. (1977). Subantarctic mode water. In a Voyage of discovery, *Deep Sea Research* (vol. *24*, pp. 103–119).

McDonagh, E. L., & King, B. A. (2005). Oceanic fluxes in the South Atlantic. *Journal of Physical Oceanography*, *35*(1), 109–122. https://doi.org/10.1175/JPO-2666.1

McDonagh, E. L., McLeod, P., King, B. A., Bryden, H. L., & Valdés, S. T. (2010). Circulation, heat, and freshwater transport at 36 N in the Atlantic. *Journal of Physical Oceanography*, *40*(12), 2661–2678. https://doi.org/10.1175/2010JPO4176.1

McDougall, T. J. & P. M. Barker, (2011):*Getting started with TEOS-10 and the Gibbs Seawater (GSW) Oceanographic Toolbox* (pp. 28). SCOR/IAPSO WG127, ISBN 978-0-646-55621-5.

McDougall, T. J., & Ferrari, R. (2017). Abyssal upwelling and downwelling driven by near-boundary mixing. *Journal of Physical Oceanography*, *47*(2), 261–283. https://doi.org/10.1175/JPO-D-16-0082.1

Meinen, C. S., Garzoli, S. L., Perez, R. C., Campos, E., Piola, A. R., Chidichimo, M. P., Dong, S., et al. (2017). Characteristics and causes of deep western boundary current transport variability at 34.5°S during 2009–2014. *Ocean Science*, *13*, 175–194. https://doi.org/10.5194/os-13-175-2017

Meinen, C. S., Speich, S., Perez, R. C., Dong, S., Piola, A. R., Garzoli, S. L., & Campos, E. J. (2013). Temporal variability of the meridional overturning circulation at 34.5°S: Results from two pilot boundary arrays in the South Atlantic. *Journal of Geophysical Research: Oceans*, *118*(12), 6461–6478. https://doi.org/10.1002/2013JC009228

Meinen, C. S., Speich, S., Piola, A. R., Ansorge, I., Campos, E., Kersalé, M., & Perez, R. C. (2018). Meridional overturning circulation transport variability at 34.5 S during 2009–2017: Baroclinic and barotropic flows and the dueling influence of the boundaries. *Geophysical Research Letters*, *45*(9), 4180–4188. https://doi.org/10.1029/2018GL077408

Orsi, A. H., Johnson, G. C., & Bullister, J. L. (1999). Circulation, mixing, and production of Antarctic bottom water. *Progress in Oceanography*, *43*(1), 55–109. https://doi.org/10.1016/S0079-6611(99)00004-X

Orsi, A. H., Whitworth, T., III, & Nowlin, W. D., Jr (1995). On the meridional extent and fronts of the Antarctic circumpolar current. *Deep Sea Research Part I: Oceanographic Research Papers*, *42*(5), 641–673. https://doi.org/10.1016/0967-0637(95)00021-W

Ou, H. W., &De Ruijter, W. P., (1986). Separation of an inertial boundary current from a curved coastline. *Journal of Physical Oceanography*, *16*(2), 280–289. https://doi.org/10.1175/1520-0485(1986)016<0280:SOAIBC>2.0.CO;2

Perez, R. C., Garzoli, S. L., Meinen, C. S., & Matano, R. P. (2011). Geostrophic velocity measurement techniques for the meridional overturning circulation and meridional heat transport in the South Atlantic. *Journal of Atmospheric and Oceanic Technology*, *28*(11), 1504–1521. https://doi.org/10.1175/JTECH-D-11-00058.1

Peterson, R. G., & Stramma, L. (1991). Upper-level circulation in the South Atlantic Ocean. *Progress in Oceanography*, *26*(1), 1–73. https://doi.org/10.1016/0079-6611(91)90006-8

Piola, A. R., & Georgi, D. T. (1982). Circumpolar properties of Antarctic intermediate water and Subantarctic mode water. *Deep Sea Research Part A: Oceanographic Research Papers*, *29*(6), 687–711. https://doi.org/10.1016/0198-0149(82)90002-4

Piola, A. R., & Gordon, A. L. (1989). Intermediate waters in the southwest South Atlantic. *Deep-Sea Research*, *36*(1), 1–16. https://doi.org/10.1016/0198-0149(89)90015-0

Pujol, M.-I., Faugère, Y., Taburet, G., Dupuy, S., Pelloquin, C., Ablain, M., & Picot, N. (2016). DUACS DT2014: the new multi-mission altimeter data set reprocessed over 20 years. *Ocean Science*, *12*(5), 1067–1090. https://doi.org/10.5194/os-12-1067-2016

Reid, J. L. (1989). On the total geostrophic circulation of the South Atlantic Ocean: Flow patterns, tracers, and transports. *Progress in Oceanography*, *23*(3), 149–244. https://doi.org/10.1016/0079-6611(89)90001-3

Reid, J. L., Nowlin, W. D., & Patzert, W. C. (1977). On the characteristics and circulation of the southwestern Atlantic Ocean. *Journal of Physical Oceanography*, *7*, 62–91. https://doi.org/10.1175/1520-0485(1977)007<0062:OTCACO>2.0.CO;2

Rintoul, S. R. (1991). South Atlantic interbasin exchange. *Journal of Geophysical Research: Oceans*, *96*(C2), 2675–2692. https://doi.org/10.1029/90JC02422

Rusciano, E., Speich, S., & Ollitrault, M. (2012). Interocean exchanges and the spreading of Antarctic intermediate water south of Africa. *Journal of Geophysical Research: Oceans*, *117*(C10). https://doi.org/10.1029/2012JC008266

Schmid, C., & Majumder, S. (2018). Transport variability of the Brazil Current from observations and a data assimilation model. *Ocean Science*, *14*(3), 417–436. https://doi.org/10.5194/os-14-417-2018

Sloyan, B. M., Wanninkhof, R., Kramp, M., Johnson, G. C., Talley, L., Tanhua, T., & Katsumata, K. (2019). The global ocean ship-base hydrographic investigations program (GO-SHIP): A platform for integrated multidisciplinary ocean science. *Frontiers in Marine Science*, *6*, 445. https://doi.org/10.3389/fmars.2019.00445

Smeed, D. A., Josey, S. A., Beaulieu, C., Johns, W. E., Moat, B. I., Frajka-Williams, E., et al. (2018). "The North Atlantic Ocean is in a state of reduced overturning.". *Geophysical Research Letters*, *45*(3), 1527–1533. https://doi.org/10.1002/2017GL076350

Smith, W., & Sandwell, D. (1997). Global sea floor topography from satellite altimetry and ship depth soundings. *Science*, *277*(5334), 1956–1962. https://doi.org/10.1126/science.277.5334.1956

Speich, S., Blanke, B., & Cai, W. (2007). Atlantic meridional overturning circulation and the Southern Hemisphere supergyre. *Geophysical Research Letters*, *34*(23). https://doi.org/10.1029/2007GL031583

Speich, S., Blanke, B., & Madec, G. (2001). Warm and cold water routes of an OGCM thermohaline conveyor belt. *Geophysical Research Letters*, *28*(2), 311–314. https://doi.org/10.1029/2000GL011748

Speich, S., Garzoli, S. L., Piola, A., Baehr, J., Baringer, M., Barreiro, M., & Chereskin, T. (2009). A monitoring system for the South Atlantic as a component of the MOC (pp. 21–25). *Proceedings of OceanObs09: Sustained ocean observations and information for society (Annex), Venice, Italy*.

Srokosz, M. A., & Bryden, H. L. (2015). Observing the Atlantic Meridional Overturning Circulation yields a decade of inevitable surprises. *Science*, *348*(6241), 1255575. https://doi.org/10.1126/science.1255575

Stramma, L., & England, M. (1999). On the water masses and mean circulation of the South Atlantic Ocean. *Journal of Geophysical Research*, *104*(C9), 20863–20883. https://doi.org/10.1029/1999JC900139

Suga, T., & Talley, L. D. (1995). Antarctic Intermediate Water circulation in the tropical and subtropical South Atlantic. *Journal of Geophysical Research*, *100*(C7), 13441–13453. https://doi.org/10.1029/95JC00858

Talley, L. D. (2003). Shallow, intermediate, and deep overturning components of the global heat budget. *Journal of Physical Oceanography*, *33*(3), 530–560. https://doi.org/10.1175/1520-0485(2003)033<0530:SIADOC>2.0.CO;2

Talley, L. D., Feely, R. A., Sloyan, B. M., Wanninkhof, R., Baringer, M. O., Bullister, J. L., & Gruber, N. (2016). Changes in ocean heat, carbon content, and ventilation: A review of the first decade of GO-SHIP global repeat hydrography. *Annual Review of Marine science*, *8*, 185–215. https://doi.org/10.1146/annurev-marine-052915-100829

Tsuchiya, M., Talley, L. D., & McCartney, M. S. (1994). Water-mass distributions in the western South Atlantic; A section from South Georgia Island (54°S) northward across the equator. *Journal of Marine Research*, *52*(1), 55–81. https://doi.org/10.1357/0022240943076759

Valla, D., Piola, A. R., Meinen, C. S., & Campos, E. (2018). Strong mixing and recirculation in the northwestern Argentine Basin. *Journal of Geophysical Research: Oceans*, *123*, 4624–4648. https://doi.org/10.1029/2018JC013907

Valla, D., Piola, A. R., Meinen, C. S., & Campos, E. (2019). Abyssal transport variations in the southwest South Atlantic: First insights from a long-term observation array at 34.5°S. *Geophysical Research Letters*, *46*, 6699–6705. https://doi.org/10.1029/2019GL082740

Visbeck, M. (2002). Deep velocity profiling using lowered acoustic Doppler current profilers: Bottom track and inverse solutions. *Journal of Atmospheric and Oceanic Technology*, *19*(5), 794–807. https://doi.org/10.1175/1520-0426(2002)019<0794:DVPULA>2.0.CO;2

Weijer, W., de Ruijter, W. P., Dijkstra, H. A., &Van Leeuwen, P. J., (1999). Impact of interbasin exchange on the Atlantic overturning circulation. *Journal of Physical Oceanography*, *29*(9), 2266–2284. https://doi.org/10.1175/1520-0485(1999)029<2266:IOIEOT>2.0.CO;2

Wunsch, C. (1996). *The ocean circulation inverse problem*. Cambridge University Press. https://doi.org/10.1017/CBO9780511629570